The production of positron emitters with millisecond half-life during helium beam radiotherapy

Ozoemelam, Ikechi Samuel; van der Graaf, Emiel R.; Brandenburg, Sytze; Dendooven, Peter

Published in:
Physics in Medicine and Biology

DOI:
10.1088/1361-6560/ab51c3

Physics in Medicine & Biology

PAPER

The production of positron emitters with millisecond half-life during helium beam radiotherapy

IOP Publishing Phys. Med. Biol. 64 (2019) 235012 (22pp) https://doi.org/10.1088/1361-6560/ab51c3

Physics in Medicine & Biology

IPEM Institute of Physics and Engineering in Medicine

PAPER

The production of positron emitters with millisecond half-life during helium beam radiotherapy

Ikechi Ozoemelam[1], Emiel van der Graaf, Sytze Brandenburg and Peter Dendooven

KVI-Center for Advanced Radiation Technology, University of Groningen, Groningen, The Netherlands

[1]Author to whom any correspondence should be addressed.

E-mail: i.s.ozoemelam@rug.nl

RECEIVED
5 July 2019

REVISED
23 October 2019

ACCEPTED FOR PUBLICATION
28 October 2019

PUBLISHED
5 December 2019

Keywords:helium therapy, monitoring, positron emission tomography, nitrogen-12, oxygen-13

Supplementary material for this article is available online

Abstract

Therapy with helium ions is currently receiving significantly increasing interest because helium ions have a sharper penumbra than protons and undergo less fragmentation than carbon ions and thus require less complicated dose calculations. For any ion of interest in hadron therapy, the accuracy of dose delivery is limited by range uncertainties. This has led to efforts by several groups to develop *in vivo* verification techniques, including positron emission tomography (PET), for monitoring of the dose delivery. Beam-on PET monitoring during proton therapy through the detection of short-lived positron emitters such as ^{12}N ($T_{1/2} = 11$ ms), an emerging PET technique, provides an attractive option given the achievable range accuracy, minimal susceptibility to biological washout and provision of near prompt feedback. Extension of this approach to helium ions requires information on the production yield of relevant short-lived positron emitters. This study presents the first measurements of the production of short-lived positron emitters in water, graphite, calcium and phosphorus targets irradiated with 59 MeV/u ^{3}He and 50 MeV/u ^{4}He beams. For these targets, the most produced short-lived nuclides are ^{13}O/^{12}N ($T_{1/2} = 8.6/11$ ms) on water, ^{13}O/^{12}N on graphite, ^{43}Ti/^{41}Sc/^{42}Sc ($T_{1/2} = 509$–680 ms) on calcium, ^{28}P ($T_{1/2} = 268$ ms) on phosphorus. A translation of the results from elemental targets to PMMA and representative tissues such as adipose tissue, muscle, compact and cortical bone, shows the dominance of ^{13}O/^{12}N in at least the first 20 s of an irradiation with ^{4}He and somewhat longer with ^{3}He. As the production of ^{13}O/^{12}N in a ^{3}He irradiation is 3–4 times higher than in a ^{4}He irradiation, from a statistical point of view, range verification using ^{13}O/^{12}N PET imaging will be about 2 times more precise for a ^{3}He irradiation compared to a ^{4}He irradiation.

1. Introduction

Hadron therapy, i.e. radiotherapy with protons and heavier ions, offers the benefit of selective deposition of a high dose to the tumour volume while reducing the co-irradiation of surrounding tissue (Paganetti 2011). The last two decades have seen a strong increase in the use of charged particles, mostly protons and carbon ions, in radiotherapy (Jermann 2015). More recently, there has been a renewed interest in the utilization of helium ions in hadron therapy (Kempe *et al* 2006, Grün *et al* 2015, Tommasino *et al* 2015, Durante and Paganetti 2016, Knäusl *et al* 2016), with implementation planned for centres such as the Heidelberg Ion Beam Therapy Center (HIT) (Krämer *et al* 2016, Mairani *et al* 2016, Tessonnier *et al* 2018). Helium ions were previously used at the Lawrence Berkeley Laboratory (LBL) in a program which spanned almost four decades and led to the treatment of more than 2000 patients (Castro *et al* 1994, Jermann 2015). The main appeal of helium ions is based on a 'middle-ground' advantage over the commonly used proton and carbon ion beams. From a physical perspective, helium ion beams show a smaller penumbra and less range straggling than proton beams (see e.g. Ströbele *et al* (2012) and Durante and Paganetti (2016)). Thus, compared to proton beams, the physical properties of helium ions ensure higher conformity of dose distributions to the target (Ströbele *et al* 2012). Although carbon ions, due to their heavier mass, allow a still smaller penumbra than helium beams, the presence of a fragmentation

tail in their depth-dose profile deteriorates the distal dose gradient of the Bragg peak (Sihver *et al* 1998). Since helium ions undergo less fragmentation than carbon ions (Rovituso *et al* 2017), they provide a good alternative for preservation of a sharp distal fall-off to negligible dose. ^{4}He ions are also being considered for mixed-particle beam treatment in combination with carbon ions, because for the same magnetic rigidity they can be accelerated together (Mazzucconi *et al* 2018). In this treatment technique, the ^{4}He ions, having three times longer range than the therapeutic carbon ions, emerge from the patient and are utilized to control the irradiation.

Similar to other ions of interest in hadron therapy, the high precision in localizing the dose maximum of helium ion beams required for accurate dose delivery poses a challenge. The localization of the dose maximum is sensitive to anatomical details and setup errors, impeding the most efficient utilization of the Bragg peak (Knopf and Lomax 2013). To allow a more accurate positioning of the Bragg peak and clinical realization of the superiority of charged particles, several techniques have been proposed for *in vivo* verification of the range of the beam (Parodi 2011, Knopf and Lomax 2013, Parodi and Polf 2018). Since the charged particles stop within the patient, a verification approach based on the detection of the primary beam as obtained in photon therapy is not possible. Most techniques for *in vivo* verification of charged particle beams involve the detection of secondary radiation created during nuclear interactions of the incident beam with the target nuclei. This secondary radiation includes the 511 keV annihilation photons following the radioactive decay of the beam-induced positron emitters (Maccabee *et al* 1969, Enghardt *et al* 2004, Nishio *et al* 2008, review papers by Studenski and Xiao (2010), Fiedler *et al* (2012) and Zhu and El Fakhri (2013)), de-excitation prompt gamma rays (Min *et al* 2006, Testa *et al* 2008, Polf *et al* 2009, Perali *et al* 2014, Hueso-González *et al* 2016, 2018, Xie *et al* 2017 among others and see review by Krimmer *et al* (2018)), secondary charged particles (Rucinski *et al* 2018). Another approach for range verification is based on the detection of beam-induced thermoacoustic waves (Hayakawa *et al* 1995, Kellnberger *et al* 2016, Patch *et al* 2016, Lehrack *et al* 2017, Jones *et al* 2018).

The most widely used technique for *in vivo* verification is the detection of annihilation gammas with positron emission tomography (PET). It is already deployed for pilot/routine clinical application in some hadron therapy centres and has been implemented in beam-on (Enghardt *et al* 2004, Ferrero *et al* 2018, Pennazio *et al* 2018), in-room (Nishio *et al* 2010, Zhu *et al* 2011) and offline (Parodi *et al* 2007, Nishio *et al* 2008, Knopf *et al* 2011, Nischwitz *et al* 2015) strategies. Although the clinical experiences have highlighted the potential of PET imaging in monitoring the beam range, the technique is still facing challenges related to the fundamental process of signal production. The signal production is not instantaneous: it occurs after a time delay which depends on the half-life of the positron emitter. The most abundant positron-emitting nuclides produced by the particle beams, ^{15}O, ^{11}C, ^{30}P, and ^{38g}K, have half-lives between 2 and 20 min, comparable to or longer than the irradiation time. In order to acquire sufficient counting statistics, data acquisition is usually performed over a considerable time interval after completion of the irradiation. Consequently, there is a delay in obtaining feedback on the treatment quality and a deterioration of the activity distribution through either metabolic washout of the positron emitters or residual activity from previous radiation fields in treatment scenarios involving several fields.

An implementation which minimizes the impact of the delay between positron emitter production and PET signal acquisition is beam-on (also called In-beam) PET (Enghardt *et al* 2004). In this strategy, the scanner is installed at the treatment position, with data collected either during the irradiation or during the beam pauses of a pulsed beam delivery. Because of their short half-lives relative to the characteristic timescales of the irradiation, the short-lived positron emitters ($T_{1/2} < 19$ s which is the half-life of ^{10}C, the shortest lived isotope relevant in existing PET implementations) are important in this beam-on strategy. The imaging of these short-lived positron emitters allows higher counting statistics in a short acquisition time, essentially avoids metabolic washout and ultimately provides quasi-prompt information on the dose delivery accuracy. In the context of proton therapy, the most important of these short-lived nuclides is ^{12}N with a half-life of 11 ms which potentially provides quasi-prompt feedback (Dendooven *et al* 2015, 2019). A recent study on the application of this nuclide for beam range monitoring during proton irradiation indicates that the range in a homogeneous target can be monitored with millimeter precision for 10^{8} protons (Buitenhuis *et al* 2017).

Currently, there is insufficient information on the production of short-lived positron emitters during helium ion therapy. To the best of our knowledge, the first experimental studies on the PET monitoring during therapy with ^{4}He beams was done in 1969 at the LBL (Maccabee *et al* 1969). Maccabee *et al* (1969) showed that positron emitting isotopes (^{11}C ($T_{1/2} = 20.3$ m), ^{15}O ($T_{1/2} = 2.05$ m), ^{18}F ($T_{1/2} = 110$ m)) are produced on graphite targets and soft tissues, and could be useful to determine the range of the beam. Due to the off-line implementation adopted in the study, the short-lived positron emitting nuclides ($T_{1/2} < 19$ s) were not detected. Similarly, an investigation of the feasibility of in-beam PET for therapeutic beams of ^{3}He by Fiedler *et al* (2006) does not mention these short-lived positron emitters. In implementing beam-on PET for helium ions, it is important to quantify the production of the short-lived positron emitters as it determines the achievable precision in range monitoring applications based on the determination of their distribution.

As a follow-up to the investigation of the production of short-lived positron emitters during irradiation with protons by Dendooven *et al* (2015), we present in this work measurements of the production of various

short-lived positron emitters during helium beam irradiation and offer insights into the potential of beam-on PET for *in vivo* dose delivery verification for helium beam therapy. Experiments using beams of both helium isotopes, ^{4}He and ^{3}He were performed.

2. Materials and methods

2.1. General consideration

In assessing the relevance of a positron emitter for PET-based monitoring of helium beams, an important factor is the yield of the positron emitter in the vicinity of the Bragg peak. This implies that a significant amount of the nuclide needs to be produced at low energy of the incident particles; at higher particle energy the nuclides are produced farther from the Bragg peak and therefore provide no information on the range. In this work we measured the production rate integrated over an energy range from zero to a beam energy corresponding to a range of 22 mm in water for both ^{4}He (50 MeV/u) and ^{3}He (59 MeV/u). Detailed measurement of the cross section versus energy, needed to simulate the reference PET image, will be the subject of follow-up investigations if justified by results of the current method.

A further consideration concerns the choice of target materials. For light ions, including helium, no positron emitters are produced via projectile fragmentation. Positron emitters are produced only by nuclear reactions on target nuclei and production depends on the elemental composition of the target. Since the production rates depend on the abundance of the target elements and given that the human body is composed predominantly of the elements oxygen, carbon, nitrogen, phosphorus, and calcium, significant contributions are expected from oxygen and carbon due to their high abundance in soft tissue. Nitrogen is not considered in this work as it has a much lower abundance than carbon and oxygen. Phosphorus and calcium are included in this work due to their relatively high abundance in bone tissue.

As a consequence of the foregoing considerations, we measured the integral production yield of positron emitters for beams of ^{3}He and ^{4}He incident on targets of carbon, water, phosphorus and calcium. Although our main emphasis is on the short-lived positron emitters, we have included the longer-lived ones to provide the necessary context on the relevance of the short-lived nuclides.

2.2. An overview of the method

The production rate of positron emitters can be determined via the measurement of the intensities of the 511 keV annihilation photons following their decay. The identification of the produced nuclides is obtained by following the decay over a certain time period and disentangling the contributions of the nuclides on the basis of their known half-lives. In order to implement this approach and provide sufficient counting statistics, the helium beam is delivered in a number of successive cycles, with each cycle composed of a beam-on and beam-off period. The beam-on/off periods were chosen to optimize the production and identification of the short-lived nuclides of interest, relative to the long-lived nuclides. A beam-on period of 2–3 times the half-life of the predominant short and/or intermediate half-life contribution was chosen to ensure a preferential production of the short-lived nuclide over the long-lived ones. To ensure a good disentangling of the individual contributions, the beam-off period of about 5 times the half-life of the short-lived nuclide under investigation was chosen. At the end of such beam-off period, the intensity of the short-lived nuclide is very small compared to the long-lived ones. Thus the contribution of the long-lived nuclides can be determined without 'interference' from the short-lived ones. As an alternative to the detection of the 511 keV annihilation photons, characteristic gamma-rays emitted by the final nucleus after positron decay can, in certain cases, be used to established the production of the positron emitter. Table 1 shows the relevant nuclides investigated in this work. Only gamma rays with branching ratios greater than 1% are indicated; in practice the detection of gamma photons with a smaller branching ratio is difficult.

2.3. Setup of beam irradiation and detector

The experiments were performed at the irradiation facility of the AGOR cyclotron at the KVI-Center for Advanced Radiation Technology (KVI-CART), University of Groningen. The AGOR cyclotron is capable of producing ^{3}He and ^{4}He ions up to a maximum energy of 120 MeV/u (range in water $R_{\text{water}} = 79.4$ mm) and 90 MeV/u ($R_{\text{water}} = 63.3$ mm), respectively. Figure 1 shows the experimental setup.

^{3}He and ^{4}He ions were accelerated to energies with the same 22 mm range in water, i.e. 59 MeV/u for ^{3}He and 50 MeV/u for ^{4}He, and delivered through the beam line vacuum window to reach targets downstream of an air-filled ionization chamber (BIM). Before the experiment, the output charge of the BIM, expressed in monitor units, was calibrated in terms of the number of individual ions counted by a scintillation detector capturing the full beam. The total number of ions delivered during an irradiation run was determined through the number of monitor units recorded by the BIM. The width of the beam as measured with a multi-wire beam profile monitor at the proximal surface of the target was 9.4 mm FWHM.

Table 1. Decay properties of positron emitters considered in this work.

Positron emitter	Half-life	Gamma ray decay data		Reference
		Energy (keV)	Branching ratio (%)	
^{8}B	770 ms		—	Tilley *et al* (2004)
^{9}C	127 ms		—	Tilley *et al* (2004)
^{10}C	19.3 s	718	100	Tilley *et al* (2004)
^{11}C	1223 s		—	Kelley *et al* (2012)
^{12}N	11.0 ms	4440	1.9	Ajzenberg-Selove (1990)
^{13}O	8.58 ms		—	Ajzenberg-Selove (1991)
^{13}N	598 s		—	Ajzenberg-Selove (1991)
^{14}O	70.6 s	2313	99.4	Ajzenberg-Selove (1991)
^{15}O	122 s		—	Ajzenberg-Selove (1991)
^{17}F	64.8 s		—	Tilley *et al* (1993)
^{18}F	6586 s		—	Tilley *et al* (1995)
^{18}Ne	1.67 s	1041	7.8	Tilley *et al* (1995)
^{19}Ne	17.3 s		—	Tilley *et al* (1995)
^{26m}Al	6.35 s		—	Basunia and Hurst (2016)
^{25}Al	7.18 s		—	Firestone (2009)
^{28}P	270 ms	1779	98	Shamsuzzoha Basunia (2013)
^{29}P	4.14 s	1273	1.3	Shamsuzzoha Basunia (2012)
^{30}P	150 s		—	Shamsuzzoha Basunia (2010)
^{30}S	1.18 s	677	78	Shamsuzzoha Basunia (2010)
^{31}S	2.55 s	1266	1.1	Ouellet and Singh (2013)
^{32}Cl	298 ms	2230	70	Ouellet and Singh (2011)
^{33}Cl	2.51 s		—	Chen and Singh (2011)
^{34}Cl	1.53 s		—	Nica and Singh (2012)
^{35}Ar	1.78 s	1219	1.4	Chen *et al* (2011)
^{37}K	1.23 s	2796	2.0	Cameron *et al* (2012)
^{38g}K	458 s	2168	100	Cameron and Singh (2008)
^{38m}K	924 ms		—	Cameron and Singh (2008)
^{38}Ca	440 ms	1568	20	Cameron and Singh (2008)
^{39}Ca	860 ms		—	Singh and Cameron (2006)
^{41}Sc	596 ms		—	Nesaraja and McCutchan (2016)
^{42g}Sc	681 ms		—	Chen and Singh (2016)
^{42m}Sc	61.7 s	437/1227/1525	100/99/100	Chen and Singh (2016)
^{42}Ti	209 ms	611	56	Chen and Singh (2016)
^{43}Ti	509 ms	845/2288	2.8/4.4	Singh and Chen (2015)

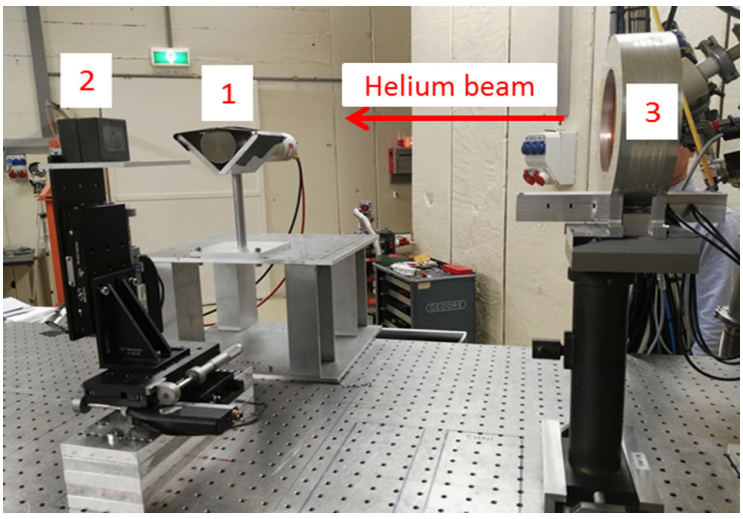

Figure 1. Experimental setup. 1: NaI detector, 2: target, 3: beam ionization monitor.

The helium ions were stopped in homogenous targets of water (H_2O), graphite, calcium and phosphorus. Table 2 summarizes the relevant information on the targets. The range of the helium particles in each target was calculated using SRIM (Ziegler *et al* 2010).

The nuclides produced in the water target will diffuse throughout the target. This is not considered a problem because the overall goal of the experiment is to measure the integral yield and not the spatial distribution. For the short-lived nuclides, diffusion has a sub-millimetre effect on the width of the positron emitter distribution. Also, the size of the water target is small enough for the diffusion of long-lived positron emitters to have a small effect on the detection efficiency.

The 511 keV annihilation photons were detected with a NaI(Tl) detector (Scionix 51B51/2M, size 51 mm × 51 mm). The detector was aligned perpendicularly to the beam direction and centered at the Bragg peak location with a distance of 25 cm between the detector front surface and the beam axis. The energy signal from the detector was sent to a spectroscopy amplifier. One amplifier output went to an ORTEC multi-channel analyser (MCA) for recording gamma ray energy spectra. The energy spectra were recorded to enable the analysis of the gamma peaks to identify nuclides with easily detectable gamma lines besides the 511 keV line. This procedure provides a more unambiguous measurement of the production of these nuclides. A second amplifier output went to a single-channel analyser (SCA) which generated a logic pulse each time the incoming signal was within the energy window of 460–630 keV set around the 511 keV full energy peak, see figure 2. These logic pulses were processed by an ORTEC multi-channel scaler (MCS), producing a time spectrum. The energy resolution of the detector at 511 keV is 7.8% sigma. Energy and time spectra were measured for several combinations of targets and beam-on/beam-off periods. The acquisition of time and energy spectra was synchronized with the beam pulsing using a dual-channel pulse generator. The pulse generator produced logical pulses used to control the electrostatic beam deflector in the cyclotron injection beam line for beam pulsing and triggering, during the beam-off periods only, the restart of the MCS cycle and data acquisition by the MCA.

The full-energy peak efficiency of the NaI detector, for the geometry of the experimental setup, was determined using ^{22}Na (511 keV and 1275 keV), ^{137}Cs (662 keV) and ^{60}Co (1173 keV and 1332 keV) gamma ray sources. The detector full-energy peak efficiency for these and for higher energy gammas was also obtained from Monte Carlo simulations using MCNPX (Pelowitz 2005). The relative agreement between measured and simulated detector efficiency is better than 10%.

2.4. Data analysis

An essential factor in determining the feasibility of PET-based *in vivo* range verification with short-lived positron emitters is the number of nuclei produced per incident particle. The number of nuclei produced per incident particle is obtained from a parametrization of the build-up and decay of the produced positron emitters during the cyclic irradiation of the target. For a stable cycle-to-cycle beam intensity, the number of positron emitters produced per second, P_i, as given in Dendooven *et al* (2015), is given as:

$$P_i = \frac{A_{o,i}}{\left(1 - e^{-\lambda_i T_{on}}\right) \sum_{m=0}^{k-1} (k-m)\, e^{-\lambda_i m \left(T_{on}+T_{off}\right)} B_{511}\varepsilon_{511}} \tag{1}$$

where λ_i is the decay constant of the positron emitter, T_{on} is the duration of the beam-on period, T_{off} is the duration of the beam-off period, k is the number of irradiation cycles, B_{511} and ε_{511} are the branching ratio and detector efficiency for the 511 keV photon. The beam-induced activity of positron emitter i at the end of the beam-on period summed over all irradiation cycles, $A_{o,i}$, was obtained as a fitting parameter from a fit of the measured activity, $A(t)$ by the following function:

$$A(t) = \sum_i A_{o,i} e^{-\lambda_i t} + C \tag{2}$$

with C representing a constant background that is added to the sum of exponentials whenever required (see section 3.1). The number of positron emitters produced per incident particle, N_i, is given by

$$N_i = \frac{P_i\ k\ T_{on}}{N_p} \tag{3}$$

where N_p is the number of particles that entered the target during the irradiation.

For nuclides which emit gamma rays after the positron decay, a gamma peak analysis was done to obtain the production per incident particle using the net counts, $N_{\gamma,i}$, in the full energy peak of the gamma line during the beam off periods. The production per incident particle, in such scenario, is given as

$$N_i = \frac{N_{\gamma,i}\ \lambda_i\ k\ T_{on}}{\left(1 - e^{-\lambda_i T_{on}}\right)\left(\sum_{m=0}^{k-1} (k-m)\, e^{-\lambda_i m \left(T_{on}+T_{off}\right)}\right)\left(1 - e^{-\lambda_i T_{off}}\right) B_\gamma \varepsilon_\gamma N_p} \tag{4}$$

where B_γ and ε_γ are the branching ratio and the detector efficiency for the gamma energy line, respectively.

Table 2. Target properties: thickness, physical form and range of the helium beams.

Target	Target thickness (g cm^{-2})	Physical form	Range (g cm^{-2})	
			59 MeV/u ^{3}He	50 MeV/u ^{4}He
Graphite	8.6	Two stacked 50 mm square, 25 mm thick graphite blocks	2.5	2.5
Water	6.6	Water-filled thin-walled truncated conical paper cup with water height = 70 mm. Beam hits conical surface of cup. Diameter at beam level ⌀ = 66 mm	2.2	2.2
Phosphorus	6.4	Red phosphorus powder pressed into a plastic cylinder. ⌀ = 50 mm and height = 35 mm. Beam hits cylindrical side surface	2.9	2.9
Calcium	4.6	Calcium granules packed into a plastic cylinder. ⌀ = 70 mm and height = 40 mm. Beam hits cylindrical side surface	2.9	2.9

3. Results

3.1. Production of positron emitters

3.1.1. Production of ^{15}O

Production of ^{15}O ($T_{1/2}$ = 122 s) is expected on both the graphite and water targets. The production of ^{15}O was investigated using a beam pulsing of 560 s on/1840 s off (3.74×10^{11} ^{3}He and 3.05×10^{11} ^{4}He ions) and 300 s on/1800 s off (1.08×10^{11} ^{3}He and 1.29×10^{11} ^{4}He ions) for graphite and water targets, respectively. Figures 3 and S1 (stacks.iop.org/PMB/64/235012/mmedia) show the spectra of the 511 keV annihilation photons as a function of time. Unless stated differently, the origin ($t = 0$) of the time axis shown in all plots is the start of the beam-on period. The beginning of the fit region for the graphite and water targets was set to 90 s and 300 s into the beam-off period to suppress contributions from nuclides with half-lives shorter than those of ^{10}C (20 s) and ^{14}O (71 s).

For the graphite targets, the production of ^{15}O is considered alongside that of ^{11}C ($T_{1/2}$ = 1223 s) and ^{13}N ($T_{1/2}$ = 598 s). A fit with ^{11}C indicates that shorter-lived nuclides contribute to the spectrum. For both ^{3}He and ^{4}He, the inclusion of ^{13}N leads to a better fit. A difference in the two spectra on graphite, however, is that while with the ^{3}He ion, no evidence of ^{15}O production on graphite is seen, a small amount of ^{15}O is produced during irradiation with ^{4}He. The absence of ^{15}O with ^{3}He can be explained by the fact that ^{15}O is the intermediate nucleus of the ^{3}He + ^{12}C reaction and therefore has a very high probability of de-excitation via emission of nucleons rather than gamma rays.

In order to obtain a more accurate determination of the production rate of the longer-lived nuclides ^{18}F, ^{11}C and ^{13}N, measurements with a longer beam-on/beam-off period (1800 s on/20 000 s off (5.06×10^{11} ^{3}He ions) and 1840 s on/8160 s off (9.75×10^{11} ^{4}He ions) for ^{3}He and ^{4}He, respectively) were made and fitting was restricted to the later parts of these spectra to exclude contributions from ^{15}O. The contribution of these long-lived nuclides in the spectra shown in figures 3 and S1 was fixed using the fit results of the longer spectrum. A constant arising from background activity was included for the water target to give a better fit.

3.1.2. Production of ^{14}O, ^{17}F, ^{19}Ne and ^{10}C

The production of ^{14}O ($T_{1/2}$ = 70.6 s) and ^{10}C ($T_{1/2}$ = 19.3 s) was investigated with a beam pulsing of 200 s on/600 s off (1.24×10^{10} ^{3}He and 1.06×10^{11} ^{4}He ions) and 150 s on/300 s off (6.45×10^{10} ^{3}He and 8.07×10^{10} ^{4}He ions) in graphite and water targets, respectively. Figure 4 shows the time spectra of the 511 keV annihilation photons. Taking into account the nuclides identified in section 3.1.1, the fit shows that ^{10}C is produced during irradiation with both ions on graphite. The previously determined contributions of the longer-lived nuclides were used in constraining their contributions for the fit of the spectra. Although the ^{14}O gamma ray was seen during irradiation with ^{3}He, inclusion of this nuclide gives a negligible contribution. This may be attributed to the fact that its production rate is within the error margins of the other nuclides. On the water target, the production of ^{17}F ($T_{1/2}$ = 64.8 s) and ^{19}Ne ($T_{1/2}$ = 17.2 s) needs to be considered alongside ^{14}O and ^{10}C. Due to the closeness of the half-lives, the analysis of the production of ^{14}O and ^{10}C on water via the decay-curve fit suffers from possible interference from potentially produced ^{17}F and ^{19}Ne, respectively. Given that both ^{14}O and ^{10}C emit easily detectable gamma rays, their production rate was obtained from the gamma peak analysis. The use of this spectral-derived value to constrain the contribution of ^{14}O and ^{10}C in the decay-curve fit allows a more accurate retrieval of the contribution of other nuclides. For ^{3}He, the production of ^{19}Ne was not observed as this is the intermediate nucleus of the ^{3}He + ^{16}O reaction. The spectra from the water target clearly indicate that ^{17}F is produced in addition to a rather small contribution from ^{14}O (not shown in the figure).

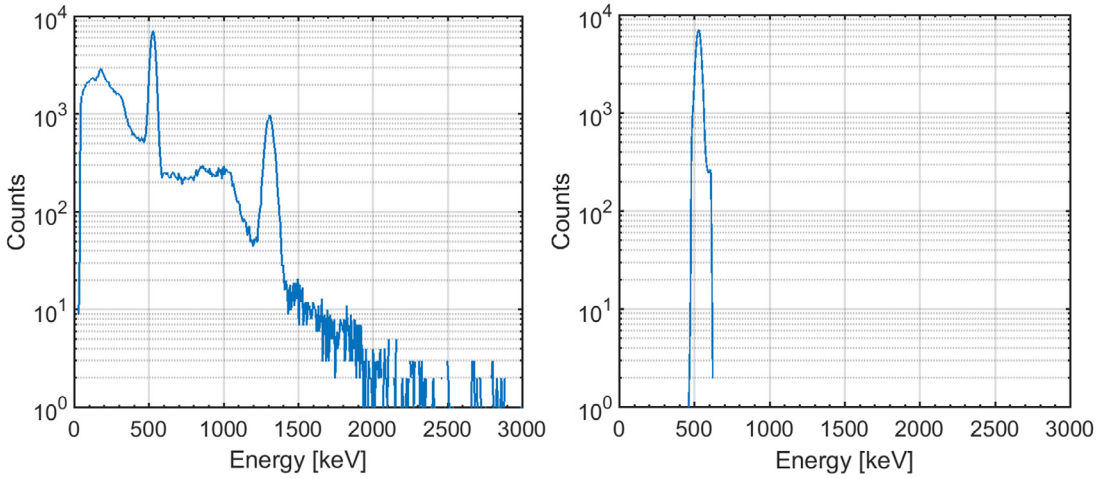

Figure 2. Selection of annihilation events. Energy spectrum (Left) of a ^{22}Na source showing the 511 keV and the 1275 keV full energy peaks. Only counts within the 511 keV energy window (right) are transmitted to the MCS for time spectrum measurement.

For irradiation of water with ^{4}He, no evidence of the production of ^{10}C is seen in the gamma spectrum. Given that the ^{14}O gamma ray is seen in the gamma spectrum, its contribution in the decay fit was constrained using the production rate determined from the gamma ray energy spectra. The inclusion of both ^{19}Ne and ^{17}F in the fit indicates an insignificant contribution of ^{19}Ne (54 $\pm$ 23 counts s^{-1}). Fitting these nuclides separately to the spectrum gives a better reduced χ^2 for ^{17}F (reduced $\chi^2 = 1.00$, DoF (degrees of freedom) $= 289$) compared to ^{19}Ne (reduced $\chi^2 = 2.13$, DoF $= 289$). We conclude that ^{19}Ne (not shown in the figure) is not produced in measurable quantities.

3.1.3. *Production of ^{18}Ne*

The production of ^{18}Ne ($T_{1/2} = 1.67$ s) in water was investigated with a beam pulsing of 4 s on/10 s off (6.28×10^{10} ^{3}He and 1.29×10^{11} ^{4}He ions) for both ^{3}He and ^{4}He ions. In figure S2, the time spectra of the 511 keV annihilation photons are shown. In addition to ^{18}Ne, the longer-lived nuclides identified in sections 3.1.1 and 3.1.2 should also be considered in the fitting of this spectrum. Thus the contributions of the longer-lived nuclides were constrained by their previously identified intensities, fitting only the ^{18}Ne intensity. For both ^{3}He and ^{4}He, the time spectrum shows that some ^{18}Ne is produced.

3.1.4. *Production of ^{9}C*

The production of ^{9}C ($T_{1/2} = 126.5$ ms) in graphite targets irradiated with ^{3}He and ^{4}He ions was investigated using a pulsing scheme of 250 ms on/750 ms off (2.96×10^{10} ^{3}He and 2.56×10^{10} ^{4}He ions). Figure S3 shows the time spectra of the 511 keV annihilation photons. The contributions of other nuclides produced on carbon can be considered to be constant on the time scale of the beam-off period. Thus, we fitted the time spectrum of the 511 keV intensity with decay with the ^{9}C half-life and a constant. Because of the possible contributions of ^{12}N and ^{13}O ($T_{1/2} = 11$ and 8.58 ms, respectively) (see section 3.1.6), the first 50 ms was excluded from the fit region. For ^{3}He, a contribution from ^{9}C of 130 $\pm$ 18 counts/10 ms is obtained at the end of the beam-on period. This demonstrates that ^{9}C is produced. For irradiation with ^{4}He, however, the fit does not suggest a contribution of ^{9}C as its value of 16 $\pm$ 8 counts/10 ms is consistent with zero. We therefore conclude that ^{9}C is not produced with ^{4}He ions and place an upper limit using a value of the fit parameter for ^{9}C of 24 counts/10 ms (value + 1σ).

3.1.5. *Production of ^{8}B*

The production of ^{8}B ($T_{1/2} = 770$ ms) on a graphite target was investigated using a beam pulsing of 2 s on/4 s off (1.01×10^{11} ^{3}He and 5.33×10^{10} ^{4}He ions). Figure S4 shows the time spectra of the 511 keV annihilation photons. In addition to ^{8}B, the nuclides identified in previous fits, ^{9}C, ^{10}C and ^{11}C need to be included in the fit. Inclusion of these nuclides in the time spectrum following irradiation with ^{3}He, however, leads to a fit with negative contribution of ^{9}C. The poor fit when including ^{11}C is related to its almost negligible contribution given the short duration of the pulsing cycle and the total irradiation time (180 s) relative to the half-life of ^{11}C ($T_{1/2} = 1223$ s). Substituting the contributions of ^{10}C and ^{11}C with a constant gives a similar result. ^{9}C and ^{10}C, identified in sections 3.1.2 and 3.1.4, respectively, should give significant contributions on this time-scale. Therefore, consistency demands their inclusion in this fit. For the ^{3}He spectrum, a better fit (with a positive ^{9}C contribution) is obtained for a combination containing ^{8}B, ^{9}C and ^{10}C (reduced $\chi^2 = 1.19$, DoF $= 74$) in contrast to one without ^{8}B (reduced $\chi^2 = 1.84$, DoF $= 75$). For the ^{4}He spectrum, there is no evidence of ^{8}B; the

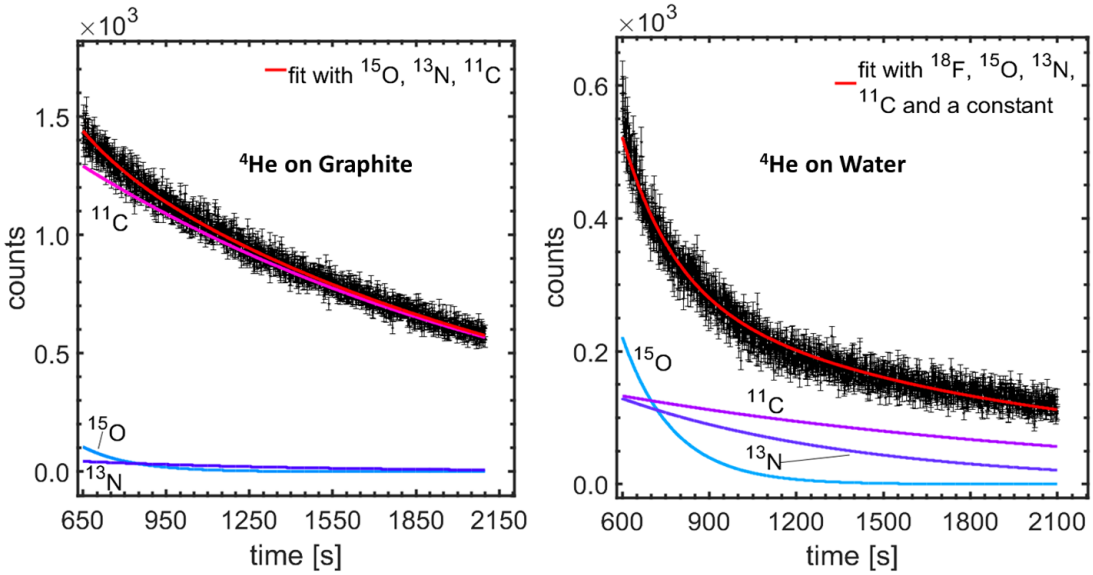

Figure 3. Spectrum of the 511 keV counts s^{-1} as a function of time during the beam-off period for ^{4}He ions in graphite target (left) and water target (right). A beam pulsing of 560 s on/1840 s off and 300 s on/1800 s off was used for the graphite and water targets, respectively. The fit of the spectrum starts 90 s and 300 s into the beam-off period for the spectra on graphite and water, respectively. The result of the fits and contributions of the indicated nuclides are shown. The small ^{18}F and constant contribution is not shown in the figure (right).

spectrum is dominated by ^{10}C. In conclusion, ^{8}B is not produced with the ^{4}He ion in measurable quantities in this experiment.

3.1.6. *Production of ^{12}N and ^{13}O*

To investigate the production of ^{12}N ($T_{1/2} = 11.00$ ms) and ^{13}O ($T_{1/2} = 8.58$ ms), a pulsing scheme of 30 ms on/60 ms off (3.22×10^{11} ^{3}He and 2.08×10^{11} ^{4}He ions on water and 2.44×10^{11} ^{3}He and 2.78×10^{11} ^{4}He ions on graphite targets) was used. The two nuclides can be produced in irradiation of both water and graphite targets with ^{3}He and ^{4}He ions. Figure 5 shows the time spectra of the 511 keV annihilation photons during the beam-off period. The origin of the time axis is the start of the beam-off period. Due to the closeness of the half-lives of these nuclides, it is impossible to disentangle their individual contributions. Therefore, the spectra are fitted only with both nuclides individually to determine the dominant nuclide contributing to the spectrum. Considering that the beam pulsing is short relative to the half-lives of the nuclides identified in the preceding sections, a constant is sufficient to represent their contribution. The first 8 ms is excluded from the fit region because we observed that there were strong fluctuations in the count rates in this period. These fluctuations, occurring during the recovery of the detector PMT from the high count rate during beam-on, are not observed beyond 8 ms.

For ^{3}He irradiations, a marginal difference between ^{12}N and ^{13}O in the goodness of the fit in both water (reduced $\chi^2 = 1.16$ versus 1.45, DoF = 51) and graphite (reduced $\chi^2 = 1.31$ versus 1.47, DoF = 51) targets is seen. The ^{4}He irradiations show a similar small difference in the χ^2 for the water (reduced $\chi^2 = 1.16$ versus 1.19, DoF = 51) and graphite (reduced $\chi^2 = 0.88$ versus 1.00, DoF = 51) targets. A definitive conclusion on the contribution of both nuclides requires further investigation, including the measurement of the 4.4 MeV gamma energy of ^{12}N (Branching ratio = 1.9%) with a high-efficiency detector, which is beyond the scope of this study. For *in vivo* range verification, however, an analytical calculation of the reference PET image using the yield of the ~10 ms contribution is sufficient. We therefore conclude for the time being that the short-lived contribution is a combination of ^{13}O and ^{12}N and indicate it from now on as ^{13}O/^{12}N.

3.1.7. *Production on a phosphorus target*

The positron emitters potentially produced during the irradiation of phosphorus with helium ions are ^{28}P($T_{1/2} = 270$ ms, $E_\gamma = 1779$ keV), ^{32}Cl($T_{1/2} = 298$ ms, $E_\gamma = 2320$ keV), ^{30}S($T_{1/2} = 1.2$ s, $E_\gamma = 677$ keV), ^{34}Cl($T_{1/2} = 1.5$ s), ^{33}Cl($T_{1/2} = 2.5$ s), ^{31}S($T_{1/2} = 2.6$ s, $E_\gamma = 1266$ keV), ^{29}P($T_{1/2} = 4.1$ s, $E_\gamma = 1273$ keV), ^{26m}Al($T_{1/2} = 6.4$ s), ^{25}Al($T_{1/2} = 7.2$ s), and ^{30}P($T_{1/2} = 150$ s). The production of these nuclides was investigated using a pulsing scheme of 10 s on/50 s off (5.91×10^{10} ^{3}He and 8.06×10^{10} ^{4}He ions). Figures 6 (left) and S5 (left), show the time spectra of the 511 keV annihilation photons during the beam-off period. For both ions, the most intense gamma peak of ^{30}S was not observed in the gamma spectrum, thus supporting the exclusion of this nuclide from further consideration. For irradiation with ^{3}He ions, the intermediate nucleus of the ^{3}He + ^{31}P reaction is ^{34}Cl. As de-excitation via gamma emission is very unlikely, this nuclide is also excluded in further

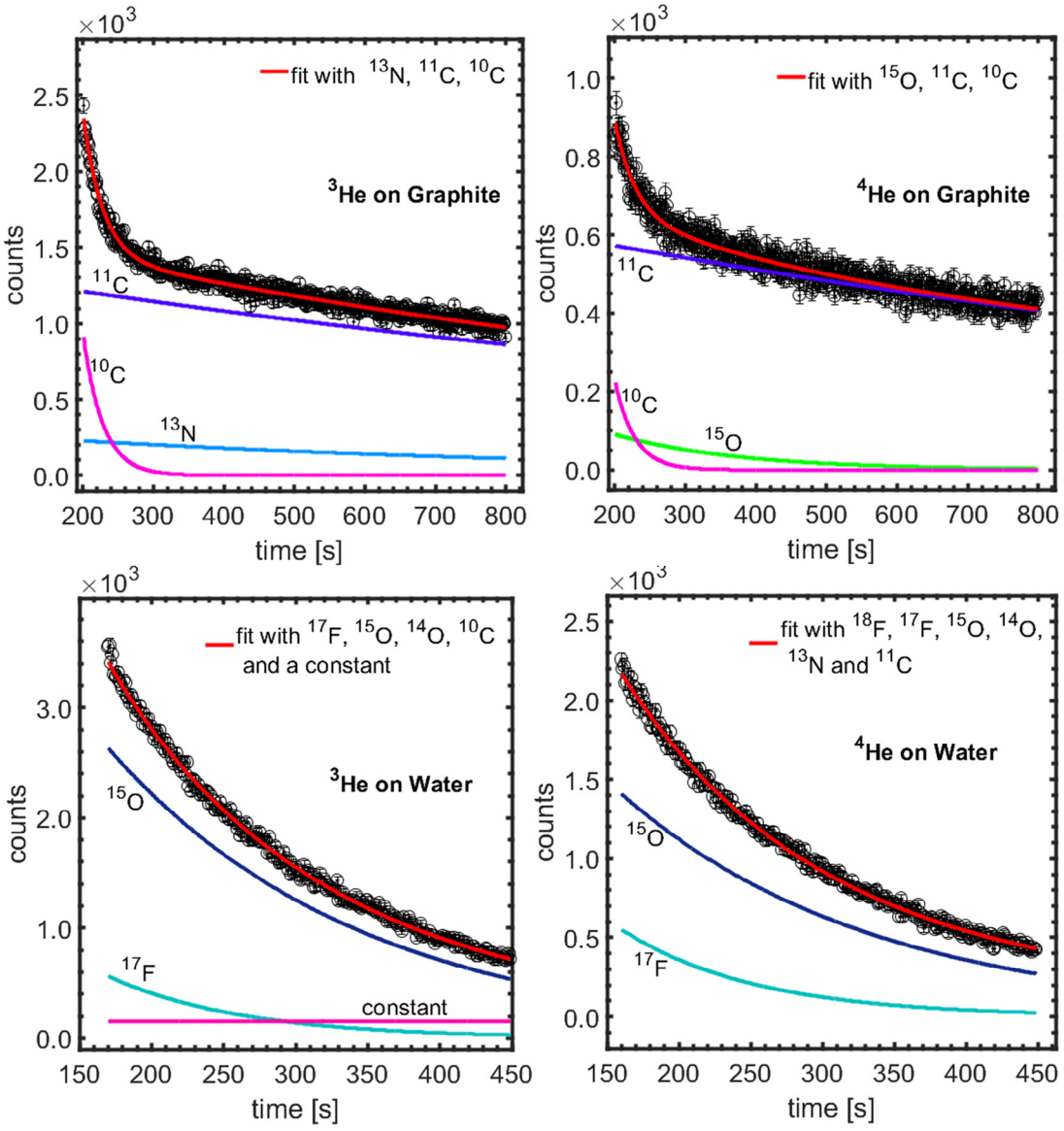

Figure 4. Spectrum of the 511 keV counts s^{-1} as a function of time during the beam-off period for ^{3}He (left) and ^{4}He (right) ions in graphite target (top) and water target (bottom). A beam pulsing of 200 s on/600 s off and 150 s on/300 s off was used for the graphite and water targets, respectively. The fit of the spectrum starts 1 s and 10–20 s into the beam-off period for the spectra on graphite and water, respectively. The result of the fits and contributions of the indicated nuclides are shown. Due to the smaller contribution of ^{14}O, ^{18}F, ^{13}N and ^{11}C in the ^{4}He on water spectra, their contributions are not shown; ^{14}O is not shown in ^{3}He on water spectra for the same reason.

analysis of the time spectrum following irradiation with ^{3}He ions. To simplify the analysis of the time spectrum, an initial fit was done starting at 20 s after the end of the beam-on period. This choice of starting point for the fit effectively excludes the contribution of nuclides with half-lives equal to or shorter than that of ^{31}S. This window was fitted with ^{30}P and each of the remaining short-lived nuclides—^{29}P, ^{26m}Al, and ^{25}Al—in separate fits. The best results, with reduced χ^2 of 1.02 and 0.92 (DoF = 298) for ^{3}He and ^{4}He irradiation, respectively, were obtained for a fit containing both ^{30}P and ^{26m}Al.

Expanding the fit window to start 1 s after the end of the beam-on period clearly shows that shorter-lived nuclides contribute to the spectrum. Therefore, these shorter-lived nuclides not included in the initial fit were individually combined with the production of ^{30}P and ^{26m}Al as obtained from the fit of the later times to ascertain the best fit. The best reduced χ^2 value was obtained for a combination containing ^{33}Cl or ^{31}S: reduced $\chi^2 = 0.98$ and 0.97, DoF = 487 for irradiation with ^{3}He and reduced $\chi^2 = 0.90$ and 0.91, DoF = 487 for irradiation with ^{4}He, respectively. The approximately equal half-lives of these short-lived nuclides precludes their simultaneous inclusion in the fit. An unequivocal conclusion as to the individual contributions necessitates the evaluation of other criteria. However, the non-observation of the ^{31}S gamma rays does not allow a definite conclusion on the absence of production of ^{31}S because of the small gamma ray branching ratio of 1.1%. Therefore, we refer to this contribution as ^{33}Cl/^{31}S.

For the very short-lived nuclides, ^{28}P and ^{32}Cl, a more specific investigation was done using a short beam pulsing of 500 ms on/1500 ms off (3.99×10^{10} ^{3}He and 3.20×10^{10} ^{4}He ions). The time spectra of the 511 keV photons are shown in figures 6 and S5 (right). Both nuclides under consideration give the same reduced χ^2 of 0.90 (DoF = 142) and 1.19 (DoF = 142) for ^{3}He and ^{4}He, respectively. As the gamma peak of ^{28}P ($E_\gamma = 1779$ keV) was observed in the gamma-ray spectrum while that of ^{32}Cl ($E_\gamma = 2231$ keV) was not seen, we conclude that only ^{28}P was produced.

We conclude that the nuclides produced during irradiation of phosphorus with ^{3}He and ^{4}He are ^{30}P, ^{26m}Al, ^{33}Cl/^{31}S and ^{28}P.

3.1.8. Production on calcium target

A fairly large number of nuclides is potentially produced on calcium. These nuclides are ^{42}Ti ($T_{1/2} = 209$ ms), ^{38}Ca ($T_{1/2} = 440$ ms), ^{43}Ti ($T_{1/2} = 509$ ms), ^{41}Sc ($T_{1/2} = 596$ ms), ^{42g}Sc ($T_{1/2} = 680$ ms), ^{39}Ca ($T_{1/2} = 860$ ms), ^{38m}K ($T_{1/2} = 925$ ms), ^{37}K ($T_{1/2} = 1.2$ s), and ^{35}Ar ($T_{1/2} = 1.8$ s), ^{42m}Sc ($T_{1/2} = 61$ s), ^{38g}K ($T_{1/2} = 462$ s). The wide range of the half-lives of these nuclides (200 ms–462 s) precludes the use of a single pulsing scheme. Therefore, we used two pulsing schemes, a long-period spectrum of 120 s on/300 s off (8.25×10^{10} ^{3}He and 1.33×10^{11} ^{4}He ions) and a short-period spectrum of 0.6 s on/3 s off (1.81×10^{10} ^{3}He and 3.26×10^{10} ^{4}He ions). Figures 7 and S6 show the time spectrum of the 511 keV photons during the beam-off period. Given the observation of the gamma lines of ^{38g}K and ^{42m}Sc (^{4}He only), the time spectrum of the long-period acquisition (figures 7 (left) and S6 (left)) was fitted with the decay constant of these long-lived nuclides. This, however, gives poor reduced χ^2 values of 16.7 and 11.3 (DoF = 298) for irradiation with ^{3}He and ^{4}He, respectively. The distribution of the fit residuals as a function of time in both fits indicates the presence of nuclides with half-lives of less than 10 s. Given that the gamma rays of ^{42}Ti and ^{38}Ca were not identified in the energy spectrum taken during beam-off, these nuclides were excluded from further consideration. The choice of nuclides, for the fit of the long-period spectrum, was further reduced by starting the fit at 2 s (3 times the half-life of ^{42g}Sc) after the end of the beam-on period. This approach suppresses the contributions of nuclides with a half-life equal to or shorter than ^{42g}Sc. Fitting any of the remaining nuclides, ^{38m}K, ^{39}Ca, ^{37}K and ^{35}Ar, gives the following reduced χ^2 of 1.10, 1.14, 1.02, and 0.97 for irradiations with ^{4}He ions and 1.22, 1.31, 1.06, and 0.99 (DoF = 295 in all fits) for irradiations with ^{3}He, respectively. The differences in the reduced χ^2 are not sufficient to provide a discrimination of the contributing nuclide(s). Thus, the spectrum in the fitting window was fitted with three contributions, ^{42m}Sc, ^{38g}K and a third contribution having its half-life as a free parameter. The fit gives a short-lived contribution with half-life of 1.67 ± 0.10 s and 1.57 ± 0.07 s for irradiation with ^{4}He and ^{3}He, respectively. The half-life obtained is closest to that of ^{35}Ar. However, it could be a combination of one or more of the short-lived nuclides considered.

Fitting the short-period spectrum with the half-life determined from the long-period spectrum and a constant gives a poor reduced χ^2 of 63.74 and 17.30 (DoF = 28 in both fits) for ^{3}He and ^{4}He, respectively. The large reduced chi-square and the trend in the fit residual indicates the presence of a shorter-lived nuclide. Given that the shorter-lived nuclides not considered so far have a small range in half-life (509–680 ms), an extra component with free half-life as a fitting parameter was included in the fit to account for their contribution. The fit gives a contribution with half-life of 550 ± 120 ms and 750 ± 190 ms for irradiations with ^{4}He and ^{3}He, respectively, consistent with the decay of any of ^{43}Ti, ^{41}Sc, and ^{42}Sc.

In conclusion, the same nuclides, the long-lived nuclides ^{38g}K and ^{42m}Sc and two short-lived contributions from any or a combination of ^{35}Ar/^{37}K/^{38m}K/^{39}Ca and ^{42g}Sc/^{41}Sc/^{43}Ti are produced during irradiation of calcium with ^{3}He and ^{4}He ions.

3.2. Corrections for escaping positrons and photon attenuation

The approach adopted in this study is based on the detection of annihilation photons which are created in the targets. However, due to their range, not all emitted positrons will annihilate in the target. As no positron absorber is inserted on the upstream surface of the target, most of the positron escape will be through this surface. Thus, the production rates measured in this study need to be corrected for positron escape. We determined the fraction of escaping positrons through Monte Carlo simulations of the positron distribution using the GEANT4 code (Agostinelli *et al* 2003). This fraction is influenced by the spatial production profile of the nuclides as well as the energy spectrum of the emitted positrons. The longitudinal spatial profile is determined by the energy dependence of the production cross section, which is unavailable for most of the nuclides considered in this study. Experimental cross sections were used to determine the spatial profile for ^{18}F (Furukawa and Tanaka 1961, Brill 1965, Nozaki *et al* 1974, Fitschen *et al* 1977), ^{11}C (^{3}He only) (Brill 1965, Cirilov *et al* 1966, Liebler *et al* 1989), ^{13}N (^{3}He only) (Cochran *et al* 1962, Brill 1965, Liebler *et al* 1989), ^{38}K (^{3}He only) (Lee and Markowitz 1974), ^{10}C (^{3}He only) (Pichard *et al* 2011), ^{42m}Sc (^{4}He only) (Rogers and Gordon 1963). For the remaining nuclides, we assumed a uniform production from the target entrance up to a depth where the beam energy is equivalent to the threshold for production of the nuclides. To model the lateral profile of the positron emitter distribution, the positron emitter source was spread according to a 2D Gaussian with a sigma of 4 mm, the helium beam width as

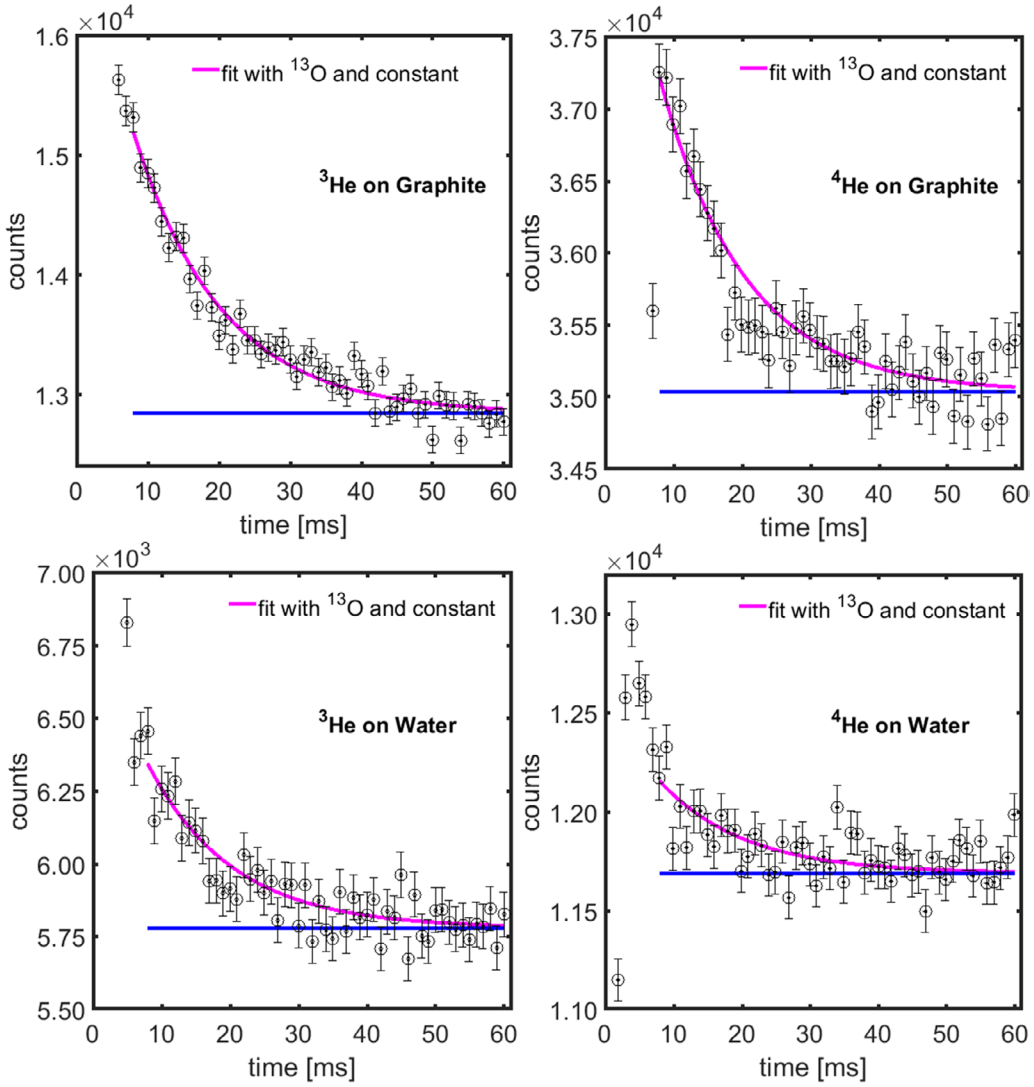

Figure 5. Spectra of the 511 keV counts ms^{-1} as a function of time during the beam-off period for ^{3}He (left) and ^{4}He (right) ions in a graphite target (top) and water target (bottom). A beam pulsing of 30 ms on/60 ms off was used. The fit of the spectrum starts 8 ms into the beam-off period to allow the detector to recover to normalcy after exposure to the high radiation environment during beam-on. The result of the fit and contributions of ^{13}O and a constant are shown.

determined with a multi-wire beam profile monitor. The energy spectrum of the positrons was calculated using the equation mentioned in Krane (1988).

The maximum energy of the positron, the branching ratio for positron emission and the escape fraction for the different nuclides are given in table 3. The uncertainty on the escape fraction was estimated to be 10%. The escape fraction is correlated with the positron endpoint energy of the nuclide. For nuclides with multiple end-point energies, a branching ratio weighted average of the escape fraction was used for corrections.

In addition to corrections for the escape of positrons, a first order correction for photon attenuation in the targets is calculated as the attenuation from the centre to the edge of the target in the direction of the detector. The attenuation of 511 keV photons for the graphite, water, phosphorus and calcium targets is 31%, 27%, 24% and 18%, respectively. The attenuation of the 2313 keV gamma ray from ^{14}O in water is 14% (production rate was determined using the gamma-peak analysis for only ^{14}O).

The production rates of positron emitting nuclides after correction for the positron branching ratio, escape fraction and photon attenuation are given in table 4. For scenarios where the decay component is attributable to a combination of nuclides, as mentioned in section 3, the half-life and escape fraction of the first nuclide in the label (^{13}O, ^{35}Ar, ^{42g}Sc, ^{33}Cl) are used for the calculation of production yields and subsequent analysis. The uncertainty due to not knowing which half-life (or half-lives) contribute to of the decay in the ^{13}O/^{12}N, ^{35}Ar/^{37}K/^{38m}K/^{39}Ca, ^{42g}Sc/^{41}Sc/^{43}Ti, and ^{33}Cl/^{31}S combinations was estimated to be 2%, 6%, 12% and 0.2%, respectively.

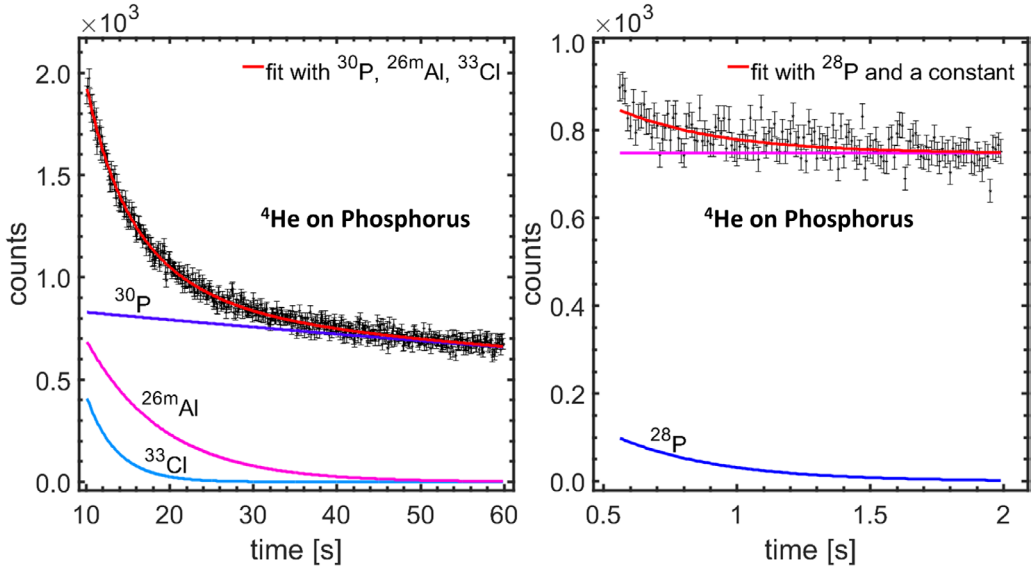

Figure 6. Spectra of the 511 keV counts/time bin as a function of time during the beam-off period for ^{4}He ions in a phosphorus target. A beam pulsing of 10 s on/50 s off (left) (time bin = 1 s) and 0.5 s on/1.5 s off (right) (time bin = 10 ms) was used. The fit of the spectrum starts 1 s (left) and 0.06 s (right) into the beam-off period. The result of the fits and contributions of the indicated nuclides are shown.

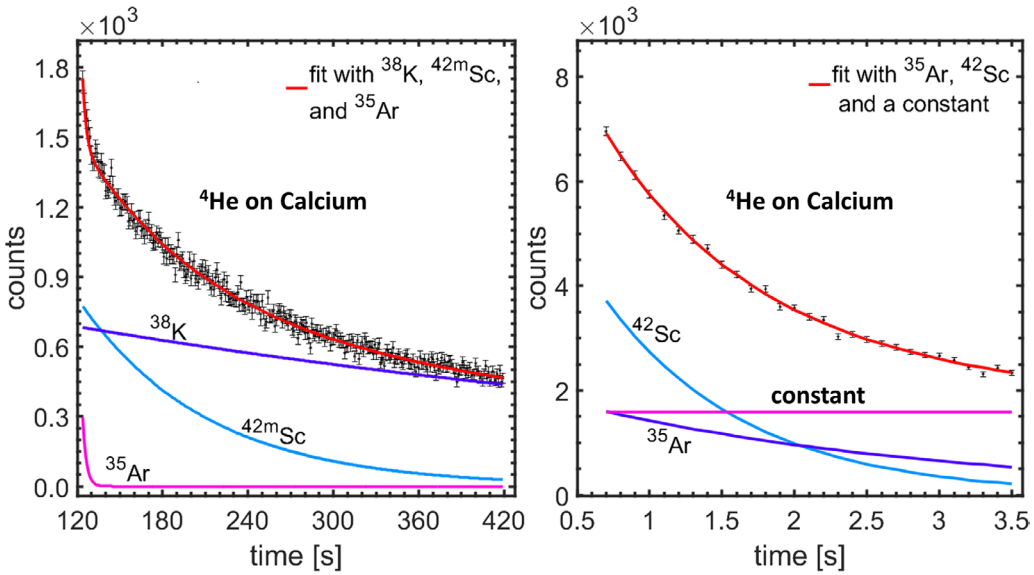

Figure 7. Spectra of the 511 keV counts/time bin as a function of time during the beam-off period for ^{4}He ions in a calcium target. A beam pulsing of 120 s on/300 s off (left) (time bin = 1 s) and 0.6 s on/3 s off (right) (time bin = 100 ms) was used. The fit of the spectrum starts 1 s (left) and 0.1 s (right) into the beam-off period. The result of the fits and contributions of the indicated nuclides are shown.

3.3. Production of PET nuclides in tissue materials and PMMA

In section 3.1, the production of positron emitting nuclides per incoming projectile in simple materials was discussed, reflecting reactions with elemental targets. In clinical applications, composite materials are encountered. In this section, we calculate the production of these nuclides in PMMA and representative tissues: adipose tissue, skeletal muscle, compact and cortical bone. We adopt a similar approach as used in Dendooven *et al* (2015).

The production per ion for any nuclide, P_{ij} is given as

$$P_{ij} = \sigma_{ij} N_j \tag{5}$$

where σ_{ij} is the cross section of the reaction leading to production of nuclide i on target nuclei of type j, and N_j is the number of target nuclei of type j cm^{-2}. A projectile traversing a target containing different elements of type j with mass number A_j, weight fractions w_j, target thickness Δx, and density ρ will encounter

$$\frac{w_j \rho \Delta x}{A_j u} = \frac{w_j}{A_j u} \frac{\Delta E}{dE/d(\rho x)} \qquad \text{nuclei of type } j \text{ per cm}^2 \tag{6}$$

where u is the atomic mass unit and $dE/d(\rho x)$ is the mass stopping power. This formula is valid if the stopping power can be considered constant over the energy loss ΔE. The ratio of the production of a nuclide via the same nuclear reaction over the same beam energy loss in two materials with weight fractions of the target nuclide w_1 and w_2 is given as

$$\frac{P_1}{P_2} = \frac{w_1}{w_2} \frac{dE/d(\rho x)_2}{dE/d(\rho x)_1}. \tag{7}$$

We used equation (7) to scale the production rate in the elemental targets to those of the representative tissues and PMMA. The stopping power in each material was calculated using SRIM (Ziegler *et al* 2010). The mass stopping power ratio of any two materials varies less than 5% from the beam energy to the production threshold energy for 59 MeV/u ^{3}He and 50 MeV/u ^{4}He ions. Table 5 gives the relevant material properties and the production per ion in these materials. The statistical and systematic uncertainties given in table 4 can be transferred to the values given in table 5.

3.4. Number of beam-on PET decays

The selection of suitable nuclides for PET-based monitoring of ion therapy depends among others on the number of decays of the positron emitting nuclides seen by the PET system. This number itself depends on the PET acquisition time structure relative to the irradiation time structure. In this section, the number of decays of the positron emitting nuclides during the irradiation of the tissues mentioned in section 3.3 is investigated. We assume a continuous helium ion irradiation. Figures 8 and 9 show the number of positron decays integrated from the beginning of the irradiation as a function of time for an irradiation with 50 MeV/u ^{4}He ions for a beam intensity of one ^{4}He ion per second. For irradiation with 59 MeV/u ^{3}He ions, the integrated number of positron decays as a function of time with a ^{3}He beam intensity of one ion per second is shown in figures S7 and S8. In these plots, we have considered only the short-lived nuclides—^{13}O/^{12}N (shown as ^{13}O in the plots) on both oxygen and carbon, ^{28}P on phosphorus, and ^{42g}Sc/^{41}Sc/^{43}Ti (shown as ^{42g}Sc in the plots) on calcium along with the most abundantly produced long-lived ones—^{15}O, ^{11}C, ^{38g}K, and ^{30}P. For each of the plots, the number of positron decays during the first second of irradiation is shown on the right side of the figures. This offers an assessment of the potential of these short-lived positron emitters to be used for prompt feedback on the irradiation quality.

4. Discussion

4.1. Benchmarking of the method

Following the findings of Dendooven *et al* (2015, 2019), the production of positron emitters during helium beam therapy is presented in this work. The integral yields of the positron emitters were obtained through the disentangling of their contributions during the pauses and/or after the end of irradiation with 59 MeV/u ^{3}He and 50 MeV/u ^{4}He beams. For nuclides with easily detectable gamma rays, a gamma ray energy analysis was performed to determine their production. To provide a benchmark of our measurement, a comparison with results derived from accurate experimental cross section data is required. For most of the nuclides produced during helium beam irradiation, no reliable (i.e. highly accurate data points in an extended energy range) cross section data is available. Since the methods in Dendooven *et al* (2019) and this work are similar, the more reliable experimental production cross section for the reactions: ^{12}C (p,pn)^{11}C and ^{12}C (p,$p2n$)^{10}C (Matsushita *et al* 2016) were used for an analytical calculation of the production yield in graphite towards validation of our method. The cross section data were interpolated at proton energies, as determined using SRIM (Ziegler *et al* 2010), equivalent to 0.5 mm steps from the target entrance to the production threshold. This calculation gives an integral yield of $(9.18 \pm 0.13_{\text{stat}} \pm 0.41_{\text{sys}}) \times 10^{-3}$ ^{11}C nuclei per 55 MeV proton and $(2.40 \pm 0.06_{\text{stat}} \pm 0.11_{\text{sys}}) \times 10^{-4}$ ^{10}C nuclei per 55 MeV proton. The uncertainties on the calculated values are projected from the experimental cross section data. In contrast, the measured values given in Dendooven *et al* (2019) are $(8.39 \pm 0.06_{\text{stat}} \pm 0.25_{\text{sys}}) \times 10^{-3}$ ^{11}C nuclei per 55 MeV proton and $(2.48 \pm 0.16_{\text{stat}} \pm 0.07_{\text{sys}}) \times 10^{-4}$ ^{10}C nuclei per 55 MeV proton. The differences between the measured and calculated values are $9\% \pm 2\%_{\text{stat}} \pm 5\%_{\text{sys}}$ and $3\% \pm 7\%_{\text{stat}} \pm 5\%_{\text{sys}}$ for the production of ^{11}C and ^{10}C, respectively. Thus, we consider an accuracy of the experimental production yield within 10% of the calculated values using experimental cross section as shown in this comparison to be a sufficient validation of the method.

4.2. Short-lived positron emitters during irradiation with helium ions

Maccabee *et al* (1969) measured the positron decay curves after the irradiation of two tissue components, graphite and soft tissue, with a 53 MeV ^{4}He beam. In these tissue components, they observed the decays from ^{15}O,

Table 3. Escape fraction of positrons emitted by positron emitting nuclides. Values are taken to be the same for nuclides produced via reactions with ^{3}He and ^{4}He ions. For the nuclide combinations, ^{13}O/^{12}N, ^{35}Ar /^{37}K/^{38m}K/^{39}Ca, ^{42g}Sc/^{41}Sc/^{43}Ti, and ^{33}Cl/^{31}S, the positron decay properties of ^{13}O, ^{35}Ar, ^{42g}Sc and ^{33}Cl were used respectively in all analysis.

Nuclide	Target	Positron endpoint energy (MeV)	Positron emission branching ratio (%)	Fraction of escaping positrons (%)
^{18}F	Water	0.63	96.7	1.2[a]
				0.3[b]
^{11}C	Water	0.96	99.8	3.9
				1.6[a]
^{13}N	Water	1.20	99.8	4.3
^{15}O	Water	1.73	99.9	5.3
^{14}O	Water	1.81	99.2	5.6
^{17}F	Water	1.73	99.9	5.3
^{10}C	Water	1.91	98.5	5.8
		0.89	1.5	3.7
^{18}Ne	Water	3.42	92.1	10
		2.38	7.7	7.4
^{13}O	Water	16.74	89.2	56
		13.24	9.8	45
^{13}O/^{12}N	Graphite	16.74	89.2	44
		13.24	9.8	34
^{13}N	Graphite	1.20	99.8	2.5
				0.6[a]
^{15}O	Graphite	1.73	99.9	3.6
^{8}B	Graphite	14.1	—	36
^{9}C	Graphite	15.47	54.1	41
		2.34	30.4	31
		12.16	5.9	6.8
		2.80	5.8	5.7
^{11}C	Graphite	0.96	99.8	2.3
				2.7[a]
^{10}C	Graphite	1.91	98.5	4.0
		0.89	1.5	0.1
				3.4[a]
^{30}P	Phosphorus	3.21	99.8	4.5
^{26m}Al	Phosphorus	3.21	99.9	4.5
^{29}P	Phosphorus	3.92	98.2	5.5
^{33}Cl	Phosphorus	4.56	99.9	6.2
^{28}P	Phosphorus	11.54	69.1	50
		4.01	11.3	7.6
		7.05	7.6	21
		4.74	3.6	9.8
		5.39	2.8	12
		5.52	2.4	13
		8.71	1.3	32
^{38g}K	Calcium	2.72	99.9	3.8
				4.2[a]
^{37}K	Calcium	5.13	97.8	8.6
^{35}Ar	Calcium	4.94	98.2	8.2
^{39}Ca	Calcium	5.51	99.9	9.9
^{42}Sc	Calcium	5.40	99.3	9.5
^{42m}Sc	Calcium	2.83	99.9	3.9
				5.7[b]

[a] Escape fraction calculated using ^{3}He experimental cross section.
[b] Escape fraction calculated using ^{4}He experimental cross section.

Table 4. Production of positron emitting nuclides per 59 MeV/u ^{3}He ion and 50 MeV/u ^{4}He ion. The statistical uncertainties are obtained from the fit of the time spectra. The systematic uncertainties are derived from the uncertainties in detector efficiency calibration and simulation of positron escape.

		^{3}He			^{4}He		
Nuclide	Target	Production per ion	Statistical uncertainty	Systematic uncertainty (%)	Production per ion	Statistical uncertainty	Systematic uncertainty (%)
^{18}F	Water	6.30×10^{-4}	7×10^{-6}	3	1.819×10^{-3}	2.1×10^{-5}	3
^{11}C	Water	3.02×10^{-3}	3×10^{-5}	3	1.579×10^{-3}	2.2×10^{-5}	3
^{13}N	Water	1.088×10^{-3}	1.3×10^{-5}	3	9.84×10^{-4}	2.4×10^{-5}	3
^{15}O	Water	8.82×10^{-3}	7×10^{-5}	3	3.414×10^{-3}	2.2×10^{-5}	3
^{14}O	Water	6.0×10^{-5}	8×10^{-6}	10	8.1×10^{-5}	1.1×10^{-5}	3
^{17}F	Water	1.47×10^{-3}	3×10^{-5}	3	1.11×10^{-3}	3×10^{-5}	3
^{10}C	Water	1.80×10^{-4}	3×10^{-5}	3	—	—	—
^{18}Ne	Water	2.02×10^{-4}	1.8×10^{-5}	4	1.88×10^{-4}	9×10^{-6}	4
^{13}O/^{12}N	Water	5.9×10^{-4}[a]	3×10^{-5}	12	2.08×10^{-4}[a]	2.8×10^{-5}	12
^{11}C	Graphite	1.328×10^{-2}	1.8×10^{-4}	3	7.34×10^{-3}	9×10^{-5}	3
^{15}O	Graphite	—		—	1.5×10^{-4}	4×10^{-5}	3
^{13}N	Graphite	1.17×10^{-3}	7×10^{-5}	3	3.84×10^{-3}	5×10^{-5}	3
^{10}C	Graphite	1.147×10^{-3}	2.1×10^{-5}	3	3.42×10^{-4}	1.6×10^{-5}	3
^{8}B	Graphite	1.424×10^{-4}	2.1×10^{-5}	7	—	—	—
^{9}C	Graphite	1.52×10^{-4}	2.1×10^{-5}	5	—	—	—
^{13}O/^{12}N	Graphite	7.10×10^{-4}[a]	2.2×10^{-5}	9	1.61×10^{-4}[a]	1.1×10^{-5}	9
^{38g}K	Calcium	3.1×10^{-3}	4×10^{-4}	3	2.59×10^{-3}	3×10^{-5}	3
^{42m}Sc	Calcium	2.29×10^{-4}	9×10^{-6}	3	6.90×10^{-4}	1.0×10^{-5}	3
^{35}Ar/^{37}K/^{38m}K/^{39}Ca	Calcium	3.63×10^{-3}[b]	1.8×10^{-4}	7	7.03×10^{-4}[b]	6×10^{-5}	7
^{42g}Sc/^{41}Sc/^{43}Ti	Calcium	2.43×10^{-3}[c]	1.0×10^{-4}	12	1.64×10^{-3}[c]	1.0×10^{-4}	12
^{30}P	Phosphorus	5.20×10^{-3}	1.7×10^{-4}	3	2.46×10^{-3}	1.2×10^{-4}	3
^{26m}Al	Phosphorus	2.03×10^{-3}	4×10^{-5}	3	9.66×10^{-4}	2.1×10^{-5}	3
^{33}Cl/^{31}S	Phosphorus	1.506×10^{-3}[d]	1.7×10^{-5}	3	8.65×10^{-4}[d]	1.0×10^{-5}	3
^{28}P	Phosphorus	2.4×10^{-4}	1.9×10^{-4}	5	2.37×10^{-4}	2.4×10^{-5}	5

[a] Production calculated using the half-life of ^{13}O.
[b] Production calculated using the half-life of ^{35}Ar.
[c] Production calculated using the half-life of ^{42g}Sc.
[d] Production calculated using the half-life of ^{33}Cl.

^{11}C and ^{18}F. Due to the delay between irradiation and measurement, shorter-lived nuclides were not observed. In the present study, we mounted the detector system at the irradiation location, thus allowing for virtually zero delay between irradiation and measurement. Further to the improvements in detector positioning, the pulsing of the beam delivery allowed the investigation of the production of short-lived nuclides down to half-lives of several milliseconds. As observed in this study, short-lived nuclides, including ^{13}O/^{12}N on both water and graphite targets with a production relative to ^{15}O and ^{11}C of 6% and 2.2%, respectively, ^{18}Ne on a water target with a production relative to ^{15}O of 6%, ^{10}C on a graphite target with a production relative to ^{11}C of 5%, ^{42g}Sc/^{41}Sc/^{43}Ti and ^{35}Ar/^{37}K/^{38m}K/^{39}Ca on a calcium target with a production relative to ^{38g}K of 63% and 27%, and ^{28}P and ^{26m}Al on a phosphorus target with a production relative to ^{30}P of 10% and 39%, respectively, are produced alongside the longer-lived nuclides mentioned in Maccabee *et al* (1969) during irradiation with ^{4}He.

Fiedler *et al* (2006) investigated the feasibility of in-beam PET for ^{3}He beams. In their study, water, graphite and PMMA targets were irradiated with varying energies of ^{3}He beams from a synchrotron with beam extraction duration and pause of about 1.4 s and 3 s, respectively. The contributions of short-lived nuclides were not evaluated as the authors assumed that the production of these nuclides is small given the small partial reaction cross sections and the long duration of the extraction pauses relative to the half-lives. The present study, however, shows that non-negligible amounts of these short-lived nuclides are produced. On water and graphite targets, the production of ^{13}O/^{12}N was observed with a production relative to ^{15}O and ^{11}C of 7% and 5%, respectively. On the water target, both ^{18}Ne and ^{10}C are produced with a production relative to ^{15}O of about 2%. While with ^{4}He ions, no evidence of the production of ^{8}B and ^{9}C on graphite target was seen, the production of these nuclides was observed in addition to ^{10}C during irradiation with ^{3}He with a production relative to ^{11}C of about 1% for both nuclides. During the irradiation with ^{3}He, the production of ^{35}Ar/^{37}K/^{38m}K/^{39}Ca and ^{42g}Sc/^{41}Sc/^{43}Ti (with a production relative to ^{38g}K of 117% and 78%, respectively) on calcium and ^{26m}Al, ^{33}Cl/^{31}S, and ^{28}P (with a production relative to ^{30}P of 39%, 29% and 5%, respectively) on phosphorus were seen.

Table 5. Production of positron emitting nuclides by 59 MeV/u ^{3}He and 50 MeV/u ^{4}He in tissues and PMMA.

Material		ICRP adipose tissue		ICRP skeletal muscle tissue		ICRU compact bone		ICRP cortical bone		PMMA			
Density (g cm^{-3})		0.92		1.04		1.85		1.85		1.19			
Weight fraction (%)		C: 63.7, O: 23.2		C: 10.8, O: 75.5		C: 27.8, O: 41.0, P: 7.0, Ca: 14.7		C: 14.4, O: 44.6, P: 10.5, Ca: 21.0		C: 60.0, O: 32.0			
Helium isotope		^{3}He	^{4}He	^{3}He	^{4}He	^{3}He	^{4}He	^{3}He	^{4}He	^{3}He	^{4}He		
Range 59/50 MeV/u ^{3}He/^{4}He ion (g cm^{-2})		2.16	2.14	2.25	2.22	2.50	2.46	2.76	2.74	2.26	2.23		
Product nuclide													
^{18}F	1.51×10^{-4}	4.56×10^{-4}		5.10×10^{-4}		1.64×10^{-3}	2.95×10^{-4}	8.59×10^{-4}	3.33×10^{-4}	9.89×10^{-4}		2.19×10^{-4}	6.37×10^{-4}
^{11}C	8.04×10^{-3}	4.59×10^{-3}		3.73×10^{-3}		2.21×10^{-3}	4.94×10^{-3}	2.70×10^{-3}	3.49×10^{-3}	1.93×10^{-3}		8.28×10^{-3}	4.55×10^{-3}
^{13}N	9.07×10^{-4}	3.30×10^{-4}		9.95×10^{-4}		9.04×10^{-4}	8.21×10^{-4}	5.04×10^{-4}	7.42×10^{-4}	5.56×10^{-4}		1.02×10^{-3}	4.24×10^{-4}
^{15}O	2.12×10^{-3}	3.05×10^{-3}		7.14×10^{-3}		3.49×10^{-3}	4.13×10^{-3}	2.63×10^{-3}	4.66×10^{-3}	2.41×10^{-3}		3.07×10^{-3}	3.28×10^{-3}
^{14}O	1.45×10^{-5}	2.04×10^{-5}		4.90×10^{-5}		7.34×10^{-5}	2.83×10^{-5}	3.84×10^{-5}	3.20×10^{-5}	4.42×10^{-5}		2.10×10^{-5}	2.85×10^{-5}
^{17}F	3.54×10^{-4}	2.79×10^{-4}		1.19×10^{-3}		1.00×10^{-3}	6.91×10^{-4}	5.26×10^{-4}	7.79×10^{-4}	6.05×10^{-4}		5.12×10^{-4}	3.90×10^{-4}
^{18}Ne	4.86×10^{-5}	4.70×10^{-5}		1.64×10^{-4}		1.69×10^{-4}	9.48×10^{-5}	8.86×10^{-5}	1.07×10^{-4}	1.02×10^{-4}		7.03×10^{-5}	6.56×10^{-5}
^{13}O/^{12}N	5.32×10^{-4}[a]	1.44×10^{-4}[a]		5.44×10^{-4}[a]		2.05×10^{-4}[a]	4.64×10^{-4}[a]	1.41×10^{-4}[a]	4.12×10^{-4}[a]	1.37×10^{-4}[a]		5.91×10^{-4}[a]	1.60×10^{-4}[a]
^{10}C	6.75×10^{-4}	1.95×10^{-4}		2.57×10^{-4}		3.66×10^{-5}	3.89×10^{-4}	9.09×10^{-5}	2.59×10^{-4}	4.98×10^{-5}		6.87×10^{-4}	1.86×10^{-4}
^{8}B	7.84×10^{-5}	—		1.38×10^{-5}	—		3.78×10^{-5}	—	2.03×10^{-5}	—		7.76×10^{-5}	—
^{9}C	8.38×10^{-5}	—		1.47×10^{-5}	—		4.04×10^{-5}	—	2.17×10^{-5}	—		8.29×10^{-5}	—
^{38g}K	1.51×10^{-4}						3.83×10^{-4}	3.15×10^{-4}	4.75×10^{-4}	3.87×10^{-4}			
^{42m}Sc							2.80×10^{-5}	8.41×10^{-5}	1.27×10^{-4}	1.04×10^{-4}			
^{35}Ar/^{37}K/^{38m}K/^{39}Ca							4.43×10^{-4}[b]	8.55×10^{-5}[b]	1.29×10^{-4}[b]	1.30×10^{-4}[b]			
^{42g}Sc/^{41}Sc/^{43}Ti							2.97×10^{-4}[c]	1.99×10^{-4}[c]	3.01×10^{-4}[c]	1.64×10^{-4}[c]			
^{30}P							3.00×10^{-4}	1.90×10^{-4}	3.02×10^{-4}	2.16×10^{-4}			
^{26m}Al							1.17×10^{-4}	7.48×10^{-5}	1.19×10^{-4}	8.52×10^{-5}			
^{33}Cl/^{31}S							8.68×10^{-5}[d]	6.70×10^{-5}[d]	1.06×10^{-4}[d]	7.63×10^{-5}[d]			
^{28}P							9.59×10^{-6}	1.84×10^{-5}	2.92×10^{-5}	8.05×10^{-5}			

[a] Production calculated using the half-life of ^{13}O.
[b] Production calculated using the half-life of ^{35}Ar.
[c] Production calculated using the half-life of ^{42g}Sc.
[d] Production calculated using the half-life of ^{33}Cl, respectively.

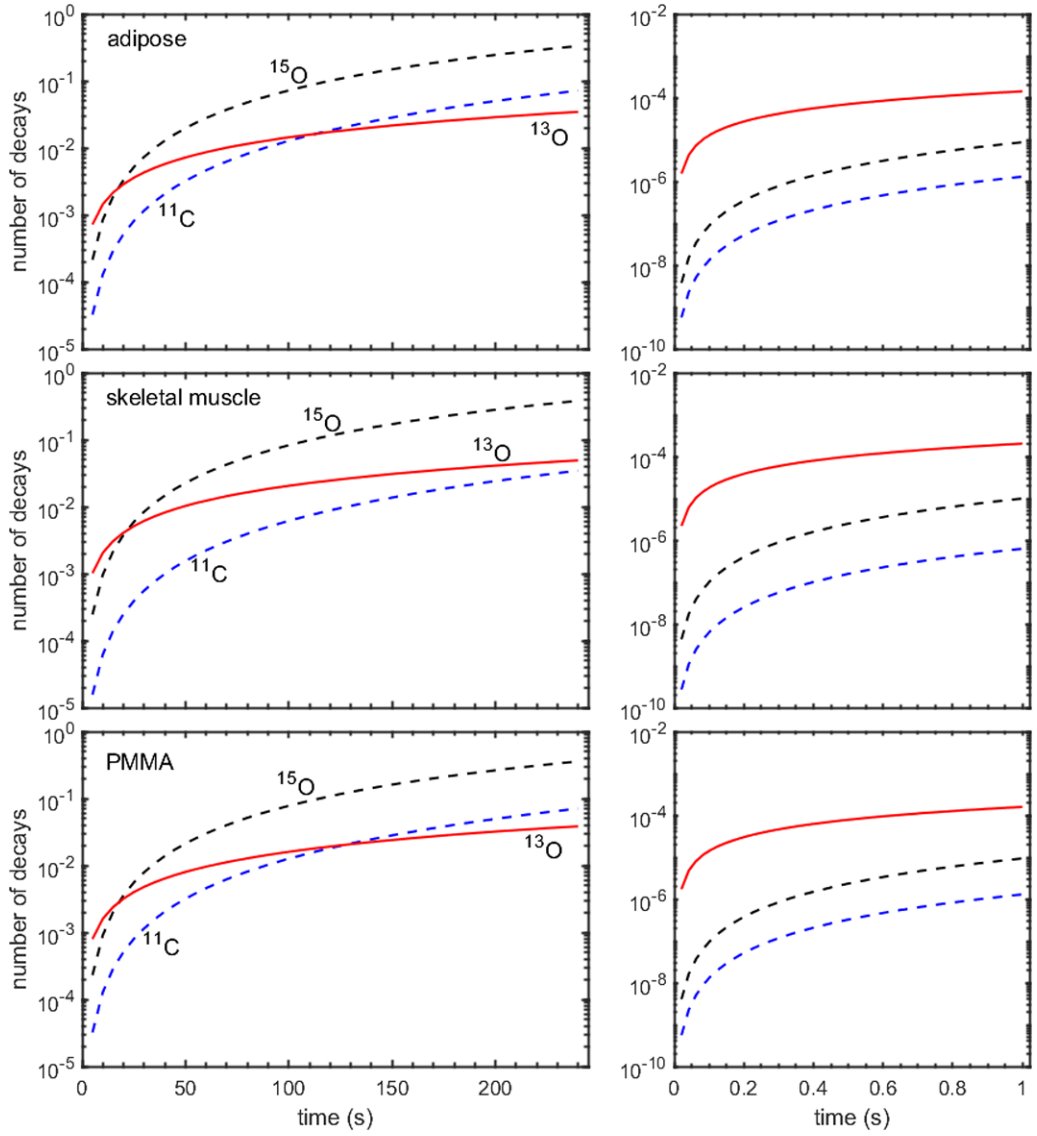

Figure 8. The number of decays of positron emitting nuclides integrated from the start of an irradiation as a function of time during the irradiation, for irradiation with 50 MeV/u ^{4}He ions and scaled to a beam intensity of 1 ion s^{-1}, for adipose, skeletal muscle, and PMMA. The plots on the right show the integrated number of decays for irradiation up to 1 s.

Dendooven *et al* (2015) identified ^{12}N as the most important very short-lived nuclide during irradiation with protons. The short half-life of ^{12}N allows feedback on dose delivery on a time scale of 50 ms, considerably shorter than the duration of a typical irradiation (Buitenhuis *et al* 2017). As mentioned in section 3.1.6, the analysis performed in this study is insufficient to conclude on the individual contributions of ^{12}N and ^{13}O to the short-lived component with a half-life of about 10 ms seen in this experiment. Nevertheless, a more important contribution from the present study for *in vivo* monitoring is that a very short-lived component, as observed during irradiation with protons, is also observed with helium ions. A corrigendum to Dendooven *et al* (2015) (Dendooven *et al* 2019) gives a production rate of ^{12}N on carbon of $4.46 \pm 0.13 \times 10^{-4}$ per 55 MeV proton. Therefore, the production of ^{13}O/^{12}N on graphite with ^{3}He is 1.6 times higher than that of ^{12}N on graphite with protons. Conversely, with ^{4}He ions, the production of ^{13}O/^{12}N on graphite is 2.8 times lower than ^{12}N on graphite with protons. Worthy of note is that the proton range in Dendooven *et al* (2019) is 20% larger than the helium range in this study. Thus, we expect 20% more production provided that the energy dependence of the production cross section for protons and helium ions is the same. Whereas no production of a very short-lived nuclide is seen during irradiation of water with protons, we observed the production of ^{13}O/^{12}N during irradiation of water with ^{3}He and ^{4}He ions with 1.3 times higher and 2.1 times smaller production rates compared to those on graphite.

4.3. Beam-on PET decays

The dominance of the PET decays from short-lived nuclides depends on their production rate relative to the longer lived ones. A further enhancement of the dominance of a short-lived nuclide is expected if the short-lived nuclide is produced on more abundant elements in the material.

For irradiation with ^{4}He, ^{13}O/^{12}N dominates the PET decays up to about 20 s in adipose, muscle and PMMA; no significant dependence of the ^{13}O/^{12}N dominance on the carbon–oxygen ratio is observed. This makes range determination quite robust with respect to the tissue type. The absence of a dependence on carbon–oxygen ratio is due to the approximately equal production rate of ^{13}O/^{12}N on carbon and oxygen.

For irradiation with ^{3}He, ^{13}O/^{12}N dominates the PET decays in oxygen-poor, carbon-rich materials for irradiation times up to 105 s in adipose tissue and 80 s in PMMA. In oxygen-rich, carbon-poor materials like skeletal muscle, ^{13}O/^{12}N dominates for irradiation times up to 25 s. This dependence of the dominance of ^{13}O/^{12}N on carbon–oxygen ratio for irradiation with ^{3}He is because ^{15}O is produced on oxygen only, in contrast to the production on both oxygen and carbon during irradiation with ^{4}He.

In addition to ^{13}O/^{12}N, other short-lived nuclides are produced during the irradiation of bone with both ^{3}He and ^{4}He ions. For irradiation with ^{4}He, ^{42g}Sc/^{41}Sc/^{43}Ti dominates the PET decays for irradiation times up to 30 s and 50 s in compact and cortical bones, respectively. For irradiations with ^{3}He, next to ^{13}O/^{12}N, ^{42g}Sc/^{41}Sc/^{43}Ti dominates the PET decays for irradiation times up to 30 s and 35 s in compact and cortical bones, respectively. The significant decays from ^{42g}Sc/^{41}Sc/^{43}Ti and ^{13}O/^{12}N in the first few seconds of irradiation in bony tissues implies that bone will become visible early on during irradiation.

All very short-lived nuclides, except ^{35}Ar/^{37}K/^{38m}K/^{39}Ca, have a (much) lower production rate than the longer-lived ones (see section 4.1). However, the much shorter half-lives result in the detection of more PET counts early on during an irradiation. The dominance of these very short-lived nuclides allows feedback on a sub-second timescale. However, the long positron ranges (directly proportional to the positron endpoint energy given in table 3) will result in the blurring of the image.

In contrast to irradiations with protons, where ^{12}N dominates the PET count for irradiation times up to 70 s and 45 s in adipose tissue and PMMA, the dominance of the short-lived nuclide ^{13}O/^{12}N is 3.5 and 2.3 times shorter for irradiation with ^{4}He in adipose tissue and PMMA, respectively, and 1.5 times longer and for a comparable duration for irradiations with ^{3}He in adipose and PMMA, respectively.

4.4. Feasibility of quasi-prompt range verification using short-lived nuclides

The production yield of ^{13}O/^{12}N in PMMA as determined in section 3.3 is 1.6×10^{-4} nuclei per ion. PET acquisition over several times the half-life of ^{13}O/^{12}N will thus result in 1.6×10^{-4} decays per ion. Crespo *et al* (2006) calculated PET scanner efficiencies for different scanner geometries, considering spheres of radioactivity of different radius. Attenuation in the phantom is not included. For a radius of activity of 50 mm, a good surrogate for imaging the distal edge of an irradiation, an *in situ* PET scanner with axial length of 32 cm, inner radius of 45.8 cm and angular coverage of 270° has a coincidence detection efficiency of about 14%. When imaging an object 20 cm in diameter, the coincidence detection efficiency will be reduced due to attenuation (assuming water as attenuating material) to about 2%, leading to the detection of 3.2×10^{-6} ^{13}O/^{12}N coincidence counts per ^{4}He ion.

In order to estimate the feasibility of ^{13}O/^{12}N-based ion range monitoring, in terms of the amount of ^{13}O/^{12}N signal produced in a treatment scenario, we refer to 'rule-of-thumb' considerations in proton pencil beam delivery provided by Zeng *et al* (2018). The spot scanning irradiation of a 1 L cube with 2 Gy (RBE) requires 2×10^{11} protons distributed over 10 000 spots in 15 layers with a maximum of 2.10×10^{8} protons in a spot. As ^{4}He ions have a factor 4 higher stopping power, a similar dose distribution, without considering differences in RBE, requires a maximum number of ^{4}He ions in a spot of 5.3×10^{7} and 3.5×10^{10} ions in the distal layer. This leads to a ^{13}O/^{12}N count of 170 and 1.1×10^{5} coincidences for a highest intensity spot and the distal energy layer, respectively, for an *in situ* PET scanner as described above.

In Buitenhuis *et al* (2017), a Monte Carlo simulation was performed to assess the precision of range verification on the basis of the imaging of ^{12}N in a graphite target. In the absence of experimental cross sections for the production of ^{12}N, the authors relied on a simplified ^{12}N distribution scaled to yield the value of 7.32×10^{-4} ^{12}N nuclei per 55 MeV proton given in Dendooven *et al* (2015). The updated ^{12}N production by protons on carbon of 4.46×10^{-4} ^{12}N nuclei per 55 MeV proton from Dendooven *et al* (2019) is a factor 1.6 smaller than the value used in the Monte Carlo simulations performed by Buitenhuis *et al* (2017). One can thus consider the results of these simulations to be valid for a number of protons that is 1.6 times higher than that quoted by Buitenhuis *et al* (2017). These simulations thus show that the range shift of a proton beam in graphite can be measured with a limited angle dual panel scanner (panel separation of 40 cm and sensitivity of 3.3% with beam activation in the centre of a graphite target block of $5 \times 5 \times 5$ cm^3) with a precision of 1.1 mm for 1.6×10^{8} protons. In the following, we use this result to estimate the precision of range verification on the basis of imaging of ^{12}N/^{13}O during helium therapy taking into consideration only the counting statistics. We assume that the beam range, target, image reconstruction algorithm and data analysis are similar to those used in Buitenhuis *et al* (2017). Other image reconstruction and data analysis methods will yield different values for the precision of range verification, but the scaling with counting statistics, the only factor we consider here, will remain valid. For 2.10×10^{8} protons in a highest intensity spot, the situation simulated by Buitenhuis *et al* (2017) will results in a precision

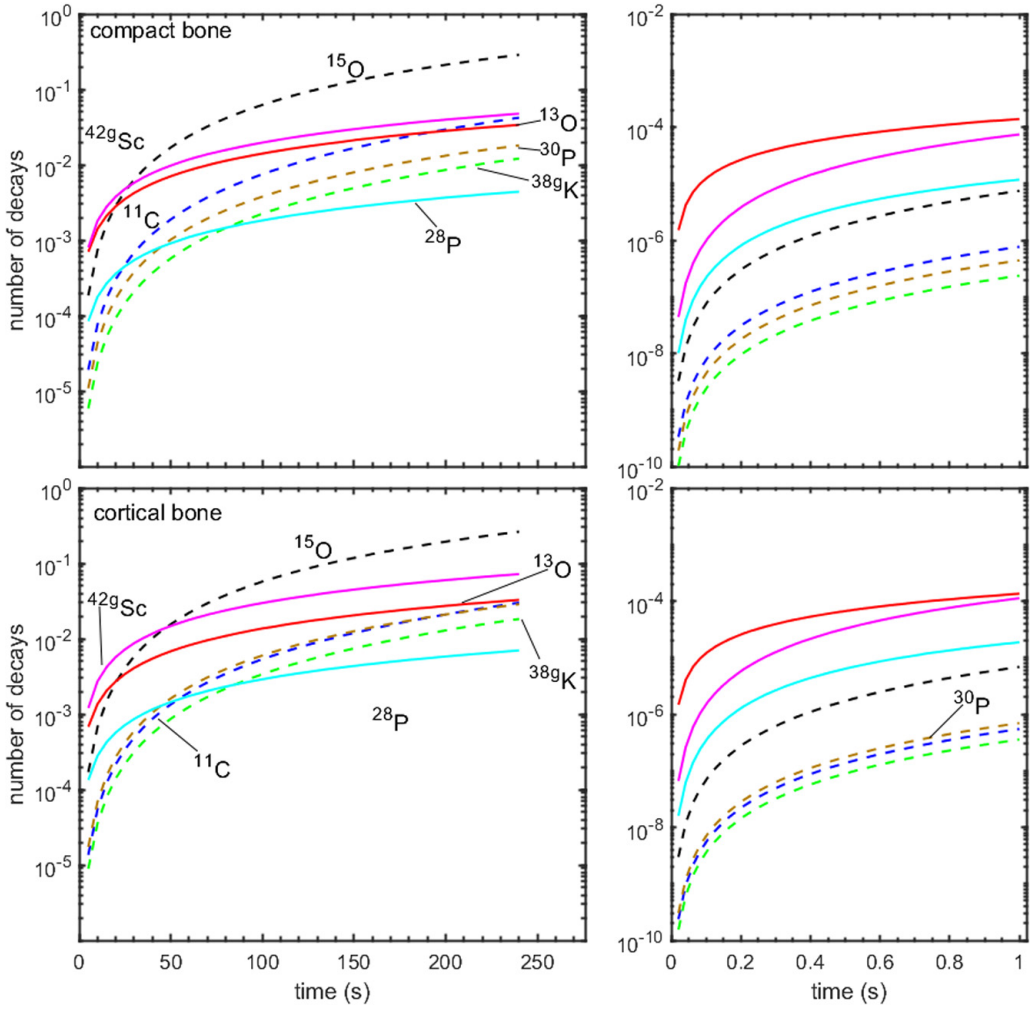

Figure 9. The number of decays of positron emitting nuclides integrated from the start of an irradiation as a function of time during the irradiation, for irradiation with 50 MeV/u ^{4}He ions and scaled to a beam intensity of 1 ion s^{-1}, for compact and cortical bone. The plots on the right show the integrated number of decays for irradiation up to 1 s.

of 1.1 x $\sqrt{1.6/2.1} = 1.0$ mm. For an imaging scenario which detects N_i PET counts, the precision of range verification scales with $\sqrt{N_i/N_0}$, where N_0 refers in this discussion to the detected counts from the simulations of Buitenhuis *et al* (2017). For a 4 times smaller number of ^{4}He particles (to achieve the same dose as for protons) and considering the 2.8 times smaller production of ^{13}O/^{12}N than with a proton beam, the number of detected PET counts will be 11.2 times smaller than that observed in Buitenhuis *et al* (2017). Thus, the precision of range verification on the basis of imaging ^{13}O/^{12}N during irradiation with ^{4}He will be $\sqrt{11.2} = 3.3$ times larger, i.e. 3.3 mm, for the highest intensity spots in the most distal layer given the scanner assumed in the simulation. For a combination of PET counts from the most distal layer following irradiation with 3.5×10^{10} ^{4}He ions, a precision of $1.0 \times \sqrt{2.8/219} = 0.11$ mm is expected using the same scanner.

In order to assess the range verification performance with a full ring system, we consider the OpenPET scanner which features two rings of 40 depth of interaction (DoI) enabled blocks of zirconium-doped gadolinium oxyorthosilicate (GSOZ) scintillators (Yoshida *et al* 2017). The rings with a diameter of 66 cm are separated by a space of 9 cm between the rings. The DoI functionality allows the use of the oblique lines of response without any loss in the spatial resolution. However, due to the large positron range of ^{12}N/^{13}O (20.8 mm RMS in water), the use of DoI detectors confers only a marginal gain in spatial resolution when imaging ^{12}N/^{13}O. Therefore, the following comparison reflects only the contribution of the scanner sensitivity to detect coincidences. The sensitivity at the centre of the field of view of the OpenPET scanner is 4.4%. When imaging a graphite target block of $5 \times 5 \times 5$ cm^3, as simulated in Buitenhuis *et al* (2017), photon attenuation of 53% in the target will reduce the sensitivity to 2.1%, leading to a 1.6 times smaller number of ^{13}O/^{12}N counts detected than with the dual panel scanner simulated in Buitenhuis *et al* (2017). Thus, it is expected that the precision for detection of range shifts in a $5 \times 5 \times 5$ cm^3 graphite target with the OpenPET scanner during irradiation with ^{4}He ions, considering only count statistics and using comparable image reconstruction and data analysis as used in Buitenhuis *et al* (2017), will be 4.1 mm and 0.14 mm for the highest intensity spots and all spots in the most distal layer, respectively.

For the materials considered in this work, the production of $^{13}O/^{12}N$ in a ^{3}He irradiation is 3 to 4 times higher than in a ^{4}He irradiation, see table 5. Consequently, from a statistical point of view, range verification using $^{13}O/^{12}N$ PET imaging will be about 2 times more precise for a ^{3}He irradiation compared to a ^{4}He irradiation.

5. Conclusion

Very short-lived positron emitters are key to the implementation of near real-time monitoring of beam delivery with PET during ion therapy. Considering the sparse information on the production of these nuclides during irradiation with helium ions, we investigated their production by irradiating water, graphite, phosphorus and calcium targets with 59 MeV/u ^{3}He and 50 MeV/u ^{4}He ions, which have the same range in the target materials. On each of these targets, the most produced very short-lived nuclides and their production relative to the long-lived nuclides are: $^{13}O/^{12}N$ ($T_{1/2} = 8.6$ ms/11.0 ms) on water (7% and 6% relative to ^{15}O for irradiation with ^{3}He and ^{4}He, respectively), $^{13}O/^{12}N$ on graphite (5% and 2% relative to ^{11}C for irradiation with ^{3}He and ^{4}He, respectively), $^{42g}Sc/^{41}Sc/^{43}Ti$ ($T_{1/2} = 509$–680 ms) on calcium (78% and 63% relative to ^{38g}K for irradiation with ^{3}He and ^{4}He, respectively), ^{28}P ($T_{1/2} = 268$ ms) on phosphorus (5% and 10% relative to ^{30}P for irradiation with ^{3}He and ^{4}He, respectively).

On the basis of the production rates obtained in this study, the expected number of counts on representative body tissues and PMMA were determined. For most of these materials, the dominantly produced nuclide is $^{13}O/^{12}N$. It dominates the PET count during the first 20 s of an irradiation with ^{4}He in adipose, muscle, and PMMA. $^{42g}Sc/^{41}Sc/^{43}Ti$ is the dominant nuclide up to 30 s and 50 s when irradiating compact and cortical bone with ^{4}He. For irradiations with ^{3}He, the PET count dominance of $^{13}O/^{12}N$ exceeds 25 s in all materials considered.

As the production of $^{13}O/^{12}N$ in a ^{3}He irradiation is 3 to 4 times higher than in a ^{4}He irradiation, from a statistical point of view, range verification using $^{13}O/^{12}N$ PET imaging will be about 2 times more accurate for a ^{3}He irradiation compared to a ^{4}He irradiation.

ORCID iDs

Ikechi Ozoemelam https://orcid.org/0000-0002-1557-7289
Emiel van der Graaf https://orcid.org/0000-0002-9254-3349
Sytze Brandenburg https://orcid.org/0000-0002-9887-1642
Peter Dendooven https://orcid.org/0000-0003-1859-1315

References

Agostinelli S *et al* 2003 Geant4—a simulation toolkit *Nucl. Instrum. Methods Phys. Res.* A **506** 250–303
Ajzenberg-Selove F 1990 Energy levels of light nuclei $A = 11$–12 *Nucl. Phys.* A **506** 1–158
Ajzenberg-Selove F 1991 Energy levels of light nuclei $A = 13$–15 *Nucl. Phys.* A **523** 1–196
Basunia M S and Hurst A M 2016 Nuclear data sheets for $A = 26$ *Nucl. Data Sheets* **134** 1–148
Brill O D 1965 Cross sections of the reactions ^{3}He with light nucleus *Yad. Fiz.* **1** 55
Buitenhuis H, Diblen F, Brzezinski K, Brandenburg S and Dendooven P 2017 Beam-on imaging of short-lived positron emitters during proton therapy *Phys. Med. Biol.* **62** 4654–72
Cameron J and Singh B 2008 Nuclear data sheets for $A = 38$ *Nucl. Data Sheets* **109** 1–170
Cameron J, Chen J, Singh B and Nica N 2012 Nuclear data sheets for $A = 37$ *Nucl. Data Sheets* **113** 365–514
Castro J R, Linstadt D E, Bahary J-P, Petti P L, Daftari I, Collier J M, Gutin P H, Gauger G and Phillips T L 1994 Experience in charged particle irradiation of tumors of the skull base: 1977–1992 *Int. J. Radiat. Oncol. Biol. Phys.* **29** 647–55
Castro J, Char D, Petti P, Daftari I, Quivey J, Singh R and Phillips T 1996 15 years' experience with helium ion radiotherapy for uveal melanoma *Int. J. Radiat. Oncol. Biol. Phys.* **36** 200
Chen J and Singh B 2011 Nuclear data sheets for $A = 33$ *Nucl. Data Sheets* **112** 1393–511
Chen J and Singh B 2016 Nuclear data sheets for $A = 42$ *Nucl. Data Sheets* **135** 1–192
Chen J, Cameron J and Singh B 2011 Nuclear data sheets for $A = 35$ *Nucl. Data Sheets* **112** 2715–850
Cirilov S, Newton J and Schapira J 1966 Total cross sections for the reaction ^{12}C ($^{3}He, \alpha$)^{11}C and ^{12}C ($^{3}He, n$)^{14}O *Nucl. Phys.* **77** 472–6
Cochran D and Knight J 1962 Excitation functions of some reactions of 6- to 24 MeV He-3 ions with carbon and aluminium *Phys. Rev.* **128** 1281–6
Crespo P, Shakirin G and Enghardt W 2006 On the detector arrangement for in-beam PET for hadron therapy monitoring *Phys. Med. Biol.* **51** 2143–63
Dendooven P, Buitenhuis H, Diblen F, Heeres P, Biegun A, Fiedler F, van Goethem M, van der Graaf E and Brandenburg S 2015 Short-lived positron emitters in beam-on PET imaging during proton therapy *Phys. Med. Biol.* **60** 8923–47
Dendooven P, Buitenhuis H, Diblen F, Heeres P, Biegun A, Fiedler F, van Goethem M, van der Graaf E and Brandenburg S 2019 Corrigendum: short-lived positron emitters in beam-on PET imaging during proton therapy (2015 *Phys. Med. Biol.* **60** 8923) *Phys. Med. Biol.* **64** 129501
Durante M and Paganetti H 2016 Nuclear physics in particle therapy: a review *Rep. Prog. Phys.* **79** 096702
Enghardt W, Crespo P, Fiedler F, Hinz R, Parodi K, Pawelke J and Pönisch F 2004 Charged hadron tumour therapy monitoring by means of PET *Nucl. Instrum. Methods Phys. Res.* A **525** 284–8
Ferrero V *et al* 2018 Online proton therapy monitoring: clinical test of a silicon-photodetector-based in-beam PET *Sci. Rep.* **8** 4100

Fiedler F, Crespo P, Parodi K, Sellesk M and Enghardt W 2006 The feasibility of in-beam PET for therapeutic beams of ^{3}He *IEEE Trans. Nucl. Sci.* **53** 2252–9
Fiedler F, Kunath D, Priegnitz M and Enghardt W 2012 Online irradiation control by means of PET *Ion Beam Therapy* ed U Linz (Berlin: Springer) p 527
Firestone R B 2009 Nuclear data sheets for $A = 25$ *Nucl. Data Sheets* **110** 1691–744
Fitschen J, Beckmann R, Holm U and Neuert H 1977 Yield and production of ^{18}F by ^{3}He irradiation of water *Int. J. Appl. Radiat. Isot.* **28** 781–4
Furukawa M and Tanaka S 1961 Excitation function for the reaction $O^{16}(a, pn)F^{18}$ *J. Phys. Soc. Japan* **16** 129
Grün R, Friedrich T, Krämer M, Zink K, Durante M, Engenhart-Cabillic R and Scholz M 2015 Assessment of potential advantages of relevant ions for particle therapy: a model based study *Med. Phys.* **42** 1037–47
Hayakawa Y, Tada J, Arai N, Hosono K, Sato M, Wagai T, Tsuji H and Tsujii H 1995 Acoustic pulse generated in a patient during treatment by pulsed proton radiation beam *Radiat. Oncol. Investig.* **3** 42–5
Hueso-González F, Fiedler F, Golnik C, Kormoll T, Pausch G, Petzoldt J, Römer K E and Enghardt W 2016 Compton camera and prompt gamma ray timing: two methods for *in vivo* range assessment in proton therapy *Frontiers Oncol.* **6**
Hueso-González F, Rabe M, Ruggieri T A, Bortfeld T and Verburg J M 2018 A full-scale clinical prototype for proton range verification using prompt gamma-ray spectroscopy *Phys. Med. Biol.* **63** 185019
Jermann M 2015 Particle Therapy Statistics in 2014 *Int. J. Part. Ther.* **2** 50–4
Jones K, Nie W, Chu J, Turian J, Kassaee A, Sehgal C and Avery S 2018 Acoustic-based proton range verification in heterogeneous tissue: simulation studies *Phys. Med. Biol.* **63** 025018
Kelley J H, Kwan E, Purcell J E, Sheu C G and Weller H R 2012 Energy levels of light nuclei $A = 11$ *Nucl. Phys.* A **880** 88–195
Kellnberger S, Assmann W, Lehrack S, Reinhardt S, Thirolf P, Queirós D, Sergiadis G, Dollinger G, Parodi K and Ntziachristos V 2016 Ionoacoustic tomography of the proton Bragg peak in combination with ultrasound and optoacoustic imaging *Sci. Rep.* **6** 29305
Kempe J, Gudowska I and Brahme A 2006 Depth absorbed dose and LET distributions of therapeutic H^{1}, He^{4}, Li^{7}, and C^{12} beams *Med. Phys.* **34** 183–92
Knäusl B, Fuchs H, Dieckmann K and Georg D 2016 Can particle beam therapy be improved using helium ions?—A planning study focusing on paediatric patients *Acta Oncol.* **55** 751–9
Knopf A and Lomax A 2013 *In vivo* proton range verification: a review *Phys. Med. Biol.* **58** R131–60
Knopf A-C, Parodi K, Paganetti H, Bortfeld T, Daartz J, Engelsman M, Liebsch N and Shih H 2011 Accuracy of proton beam range verification using post-treatment positron emission tomography/computed tomography as function of treatment site *Int. J. Radiat. Oncol. Biol. Phys.* **79** 297–304
Krämer M *et al* 2016 Helium ions for radiotherapy? Physical and biological verifications of a novel treatment modality *Med. Phys.* **43** 1995–2004
Krane K 1988 *Introductory Nuclear Physics* (New York: Wiley)
Krimmer J, Dauvergne D, Létang J M and Testa É 2018 Prompt-gamma monitoring in hadrontherapy: a review *Nucl. Instrum. Methods Phys. Res.* A **878** 58–73
Lee D and Markowitz S 1974 ^{3}He activation analysis for S, Cl, K and Ca *J. Radioanal. Chem.* **19** 159–67
Lehrack S *et al* 2017 Submillimeter ionoacoustic range determination for protons in water at a clinical synchrocyclotron *Phys. Med. Biol.* **62** L20–30
Liebler V, Bethge K, Krauskopf J, Meyer J, Misaelides P and Wolf G 1989 Determination of excitation functions for carbon detection by charged particle activation analysis *Nucl. Instrum. Methods Phys. Res.* B **36** 7–13
Maccabee H, Madhvanath U and Raju M 1969 Tissue activation studies with alpha-particle beams *Phys. Med. Biol.* **14** 213–24
Mairani A *et al* 2016 Biologically optimized helium ion plans: calculation approach and its *in vitro* validation *Phys. Med. Biol.* **61** 4283–99
Matsushita K, Nishio T, Tanaka S, Tsuneda M, Sugiura A and Ieki K 2016 Measurement of proton-induced target fragmentation cross sections in carbon *Nucl. Phys.* A **946** 104–16
Mazzucconi D, Agosteo S, Ferrarini M, Fontana L, Lante V, Pullia M and Savazzi S 2018 Mixed particle beam for simultaneous treatment and online range verification in carbon ion therapy: proof-of-concept study *Med. Phys.* **45** 5234–43
Min C, Kim C, Youn M and Kim J 2006 Prompt gamma measurements for locating the dose falloff region in the proton therapy *Appl. Phys. Lett.* **89** 183517
Nesaraja C D and McCutchan E A 2016 Nuclear data sheets for $A = 41$ *Nucl. Data Sheets* **133** 1–220
Nica N and Singh B 2012 Nuclear data sheets for $A = 34$ *Nucl. Data Sheets* **113** 1563–733
Nischwitz S *et al* 2015 Clinical implementation and range evaluation of *in vivo* PET dosimetry for particle irradiation in patients with primary glioma *Radiother. Oncol.* **115** 179–85
Nishio T, Miyatake A, Nakagawa K, Ogino T and Saijo N 2008 Development and clinical use of beam on-line PET system mounted on a rotating gantry port in proton therapy *Int. J. Radiat. Oncol. Biol. Phys.* **72** S108–9
Nishio T, Miyatake A, Ogino T, Nakagawa K, Saijo N and Esumi H 2010 The development and clinical use of a beam ON-LINE PET system mounted on a rotating gantry port in proton therapy *Int. J. Radiat. Oncol. Biol. Phys.* **76** 277–86
Nozaki T, Iwamoto M and Ido T 1974 Yield of ^{18}F for various reactions from oxygen and neon *Int. J. Appl. Radiat. Isot.* **25** 393–9
Ouellet C and Singh B 2011 Nuclear data sheets for $A = 32$ *Nucl. Data Sheets* **112** 2199–355
Ouellet C and Singh B 2013 Nuclear data sheets for $A = 31$ *Nucl. Data Sheets* **114** 209–396
Paganetti H (ed) 2011 *Proton Therapy Physics* 1st edn (Boca Raton, FL: CRC Press) pp 1–18
Parodi K 2011 *In vivo* dose verification *Proton Therapy Physics* ed H Paganetti, 1st edn (Boca Raton, FL: CRC Press) pp 489–524
Parodi K and Polf J 2018 *In vivo* range verification in particle therapy *Med. Phys.* **45** e1036–50
Parodi K *et al* 2007 Patient study of *in vivo* verification of beam delivery and range, using positron emission tomography and computed tomography imaging after proton therapy *Int. J. Radiat. Oncol. Biol. Phys.* **68** 920–34
Patch S *et al* 2016 Thermoacoustic range verification using a clinical ultrasound array provides perfectly co-registered overlay of the Bragg peak onto an ultrasound image *Phys. Med. Biol.* **61** 5621–38
Pelowitz D B 2005 MCNPX User's Manual Version 2.50 (Los Alamos, NM: Los Alamos National Laboratory) LA-CP-05-0369
Pennazio F *et al* 2018 Carbon ions beam therapy monitoring with the INSIDE in-beam PET *Phys. Med. Biol.* **63** 145018
Perali I *et al* 2014 Prompt gamma imaging of proton pencil beams at clinical dose rate *Phys. Med. Biol.* **59** 5849–71
Pichard A, Mrázek J, Assié M, Hass M, Honusek M, Lhersonneau G, de Oliveira Santos F, Saint-Laurent M-G and Šimečková E 2011 A new cross-section measurement of reactions induced by ^{3}He particles on a carbon target *Eur. Phys. J.* A **47** 72
Polf J, Peterson S, Ciangaru G, Gillin M and Beddar S 2009 Prompt gamma-ray emission from biological tissues during proton irradiation: a preliminary study *Phys. Med. Biol.* **54** 731–43
Rogers P and Gordon G 1963 Decay of Sc^{42m} and the levels of Ca^{42} *Phys. Rev.* **129** 2653–9

Rovituso M *et al* 2017 Fragmentation of 120 and 200 MeV/u ^{4}He ions in water and PMMA targets *Phys. Med. Biol.* **62** 1310–26
Rucinski A *et al* 2018 Secondary radiation measurements for particle therapy applications: charged particles produced by ^{4}He and ^{12}C ion beams in a PMMA target at large angle *Phys. Med. Biol.* **63** 055018
Shamsuzzoha Basunia M 2010 Nuclear data sheets for $A = 30$ *Nucl. Data Sheets* **111** 2331–424
Shamsuzzoha Basunia M 2012 Nuclear data sheets for $A = 29$ *Nucl. Data Sheets* **113** 909–72
Shamsuzzoha Basunia M 2013 Nuclear data sheets for $A = 28$ *Nucl. Data Sheets* **114** 1189–291
Sihver L, Schardt D and Kanai T 1998 Depth-dose distributions of high-energy carbon, oxygen and neon beams in water *Igaku Butsuri.* **18** 1–21
Singh B and Cameron J 2006 Nuclear data sheets for $A = 39$ *Nucl. Data Sheets* **107** 225–354
Singh B and Chen J 2015 Nuclear data sheets for $A = 43$ *Nucl. Data Sheets* **126** 1–150
Ströbele J, Schreiner T, Fuchs H and Georg D 2012 Comparison of basic features of proton and helium ion pencil beams in water using GATE *Z. Med. Phys.* **22** 170–8
Studenski M and Xiao Y 2010 Proton therapy dosimetry using positron emission tomography *World J. Radiol.* **2** 135
Tessonnier T, Mairani A, Chen W, Sala P, Cerutti F, Ferrari A, Haberer T, Debus J and Parodi K 2018 Proton and helium ion radiotherapy for meningioma tumors: a Monte Carlo-based treatment planning comparison *Radiat. Oncol.* **13** 2
Testa E, Bajard M, Chevallier M, Dauvergne D, Le Foulher F, Freud N, Létang J, Poizat J, Ray C and Testa M 2008 Monitoring the Bragg peak location of 73MeV/u carbon ions by means of prompt γ-ray measurements *Appl. Phys. Lett.* **93** 093506
Tilley D R, Kelleya J H, Godwina J L, Millener D J, Purcell J E, Sheua C G and Weller H R 2004 Energy levels of light nuclei $A = 8, 9, 10$ *Nucl. Phys.* A **745** 155–362
Tilley D R, Weller H R and Cheves C M 1993 Energy levels of light nuclei $A = 16$–17 *Nucl. Phys.* A **565** 1–184
Tilley D R, Weller H R, Cheves C M and Chasteler R M 1995 Energy levels of light nuclei $A = 18$–19 *Nucl. Phys.* A **595** 1–170
Tommasino F, Scifoni E and Durante M 2015 New ions for therapy *Int. J. Part. Ther.* **2** 428–38
Xie Y *et al* 2017 Prompt gamma imaging for *in vivo* range verification of pencil beam scanning proton therapy *Int. J. Radiat. Oncol. Biol. Phys.* **99** 210–8
Yoshida E, Tashima H, Shinaji T, Shimizu K, Wakizaka H, Mohammadi A, Nishikido F and Yamaya T 2017 Development of a whole-body dual ring OpenPET for in-beam PET *IEEE Trans. Radiat. Plasma Med. Sci.* **1** 293–300
Zeng C, Amos R A, Winey B, Beltran C, Saleh Z, Tochner Z, Kooy H and Both S 2018 Proton treatment planning *Target Volume Delineation and Treatment Planning for Particle Therapy: a Practical Guide* ed N Lee *et al*, 1st edn (Berlin: Springer) pp 45–105
Ziegler J, Ziegler M and Biersack J 2010 SRIM—the stopping and range of ions in matter *Nucl. Instrum. Methods Phys. Res.* B **268** 1818–23
Zhu X and El Fakhri G 2013 Proton therapy verification with PET imaging *Theranostics* **3** 731–40
Zhu X, España S, Daartz J, Liebsch N, Ouyang J, Paganetti H, Bortfeld T and El Fakhri G 2011 Monitoring proton radiation therapy with in-room PET imaging *Phys. Med. Biol.* **56** 4041–57